

# **Complete synthetic seismograms based on a spherical self-gravitating Earth model with an atmosphere-ocean-mantle-core structure**

Rongjiang Wang<sup>1\*</sup>, Sebastian Heimann<sup>1</sup>, Yong Zhang<sup>2</sup>, Hansheng Wang<sup>3</sup>, and Torsten Dahm<sup>1</sup>

1. Helmholtz Centre Potsdam, GFZ German Research Centre for Geosciences, 14473 Potsdam, Germany
2. School of Earth and Space Sciences, Peking University, Beijing 100871, China
3. State Key Laboratory of Geodesy and Earth's Dynamics, Institute of Geodesy and Geophysics, Chinese Academy of Sciences, Wuhan 430077, China

## **Abstract**

A hybrid method is proposed to calculate complete synthetic seismograms based on a spherically symmetric and self-gravitating Earth with a multi-layered structure of atmosphere, ocean, mantle, liquid core and solid core. For large wavelengths, a numerical scheme is used to solve the geodynamic boundary-value problem without any approximation on the deformation and gravity coupling. With decreasing wavelength, the gravity effect on the deformation becomes negligible and the analytical propagator scheme can be used. Many useful approaches are used to overcome the numerical problems that may arise in both analytical and numerical schemes. Some of these approaches have been established in the seismological community and the others are developed for the first time. Based on the stable and efficient hybrid algorithm, an all-in-one code QSSP is implemented to cover the complete spectrum of seismological interests. The performance of the code is demonstrated by various tests including the curvature effect on teleseismic body and surface waves, the appearance of multiple reflected, teleseismic core phases, the gravity effect on long period surface waves and free oscillations, the simulation of near-field displacement seismograms with the static offset, the coupling of tsunami and infrasound waves, and free oscillations of the solid Earth, the atmosphere and the ocean. QSSP is open source software that can be used as a stand-alone

FORTTRAN code or may be applied in combination with a Python toolbox to calculate and handle Green's function databases for efficient coding of source inversion problems.

Keywords: Acoustic-gravity waves, Surface waves and free oscillations, theoretical seismology, wave propagation, computational seismology, body waves

## **1. Introduction**

The efficient calculation of complete wave fields of displacement, tilt, strain or stress in a broad frequency band (e.g., from DC to 2 Hz), generated by point sources in different layers of the Earth, is still of great scientific interest, although different solutions have been presented in the past for specific wave modes or frequency ranges. The geodynamic boundary-value problem can be solved based on a spherically symmetric Earth model, for which semi-analytical solutions are available. In many cases, the semi-analytical solutions are sufficiently accurate for interpreting the observations. In other cases, they can provide a good reference for heterogeneous 3D Earth models.

The semi-analytical solutions are commonly obtained with the spectral method. Making a Fourier (Laplace) transform with respect to the time variable and expanding the frequency-domain observables (displacement-stress vector) into spherical harmonics, the partial differential equations of motion are converted to a set of ordinary differential equations governing the spectral observables as functions of radius (depth). The latter can be solved using either the propagator or numerical integration approach, depending on whether all fundamental solutions exist for each homogeneous spherical shell. The time-space domain solutions are obtained finally by the summation of weighted spherical harmonics and inverse Fourier (Laplace) transform.

For seismological applications, there have been various semi-analytical modelling tools based on spherical Earth models. Some of them were developed to calculate the static

deformation and gravity changes caused by dislocation sources (Pollitz, 1992, 1997; Okubo, 1993; Sun and Okubo, 1993, 1998). These tools differ mainly in whether an analytical propagator or a numerical integration approach is used to solve the ordinary differential equations. In order to model seismic deformation at local to regional scales, the corresponding tools based on the half-space geometry were developed in parallel to those based on the spherical geometry. For example, the analytical closed-form dislocation model based on a homogeneous elastic half-space (Okada, 1992) is most widely used to analyse near-field geodetic observations. For large-scale earthquakes whose deformation field may be modified by the structure below the seismogenic zone, the semi-analytical tools based on a multi-layered elastic or viscoelastic half-space are often used (Rundle, 1980, 1981, 1982; Wang et al., 2003, 2006).

The other tools, which are in the interest of the present paper, are those for generating complete synthetic seismograms, such as the reflectivity method (Fuchs, 1968; Fuchs and Müller, 1971; Kennett, 1983; Müller, 1985) or the orthonormal propagator method (Chapman and Phinney, 1972; Wang, 1999; Chapman, 2003) with improved computational efficiency. Here, it is important to recognize that nearly complete seismograms at teleseismic distances on a spherical Earth can also be generated using a layered half-space model by applying the so-called earth-flattening transformation (Müller, 1985) to the seismic material parameters. However, this approximation usually breaks down for very large distances ( $\geq 120^\circ$ ) and for rays with turning points in the inner core.

Many corresponding tools for synthetic seismograms have been developed recently based on spherical Earth models (Friederich and Dalkolmo, 1995; Kawai et al., 2006; Al-Attar and Woodhouse, 2008; Yang et al. 2010; Masters et al., 2011; van Driel et al. 2015). We mention two of them that are widely used currently in the seismological community: MINEOS written by Masters et al. (2011) and GEMINI written by Friederich and Dalkolmo (1995). MINEOS calculates eigenfrequencies and eigenfunctions of a spherically symmetric

and self-gravitating Earth model (Gilbert and Backus, 1966, 1968) and then generate low-frequency ( $\leq 0.15$  Hz) seismograms through the normal mode summation. As a complementary to MINEOS, GEMINI uses the frequency-domain integration method, which is recommended to calculate complete synthetic seismograms at higher frequency (up to 1-2 Hz).

In mathematics, the spectral methods applied to the spherical and half-space geometries differ in the way that the former uses a discrete series of spherical harmonics and the latter uses a continuous spectrum of cylindrical harmonics to represent the spatial variations of observables. Under certain assumptions, the time-space-domain results from any two corresponding spherical and half-space models are in principle comparable. Cross checks between them are useful to find bugs and clarify limitations existing in different program codes.

It is recognized that also the semi-analytical tools may involve different numerical problems. In particular, unstable results may be caused by (1) degeneration of fundamental solutions at the dynamic-to-static transition and in other extreme cases, (2) the effect of the Brunt-Väisälä (buoyancy) frequency existing in the liquid core, ocean and atmosphere, (3) loss of precision when using the traditional propagator algorithm at short wavelengths, (4) slow convergence when the source and receiver are located at close depths, and (5) time-domain and space-domain aliasing. Though there have been many techniques to overcome these numerical difficulties, they are not systematically implemented in the existing tools mentioned above. Moreover, the different tools were developed for specific purposes with some limitations. For example, though static deformation can be determined directly from the permanent offset of a complete displacement seismogram, it often needs to be calculated with an independent static dislocation tool because of numerical efficiency and stability. Besides, complete synthetic seismograms are almost always generated for a solid Earth and therefore they generally do not include oceanic tsunami and atmospheric acoustic-infrasound waves.

In this paper we present a new method to calculate complete seismograms based on a non-rotating, spherically symmetric, isotropic linear elastic and self-gravitating Earth with a multi-layered structure of the atmosphere, ocean, mantle, liquid core and solid core. The term “complete” means that all seismic signals, which exist physically for the assumed model and are numerically significant at the spatial and temporal scales selected by users, are included with sufficient accuracy. In the present case, it includes static offset, free oscillations of the solid Earth and the atmosphere and the ocean, body and surface waves, tsunami and acoustic-infrasound waves, etc. Based on this method, an all-in-one code, called QSSP, was implemented and has been updated several times over last few years. Actually, the performance of QSSP has been tested with GEMINI (Friederich and Dalkolmo, 1995) and QSEIS (Wang, 1999). The current version of QSSP is used routinely for generating Green’s function databases for seismic source inversion (e.g., Heimann et al., 2013; Zhang et al., 2014a, b; Schurr et al., 2014). Other applications of QSSP are demonstrated, for example, by Ivan and Wang (2013) and Ivan et al. (2015) for comparison of observed seismic phases  $P_{dif}$  and  $P5KP$  with their synthetics, and by Raveloson et al. (2012) for simulating infrasound gravity waves induced by the great 2004 Indian Ocean tsunami. Further application examples and cross checks with other tools are demonstrated in this paper after a comprehensive introduction to the basic theory and a detailed description of the algorithm used in QSSP. The new methods can be used by scientists and seismologists for the modelling of wave fields or the inversion of seismic sources in the Earth or in other planets, but it is also recommended for routine automatic applications because of its efficiency and robustness.

## 2. Theory

In this study, we are interested in the complete deformation process induced by an earthquake in a spherically symmetric, elastic and self-gravitating Earth. The equations of motion governing the geodynamic process are described in Appendix A. By means of the Fourier (Laplace) transform and the spherical harmonic expansion, the partial differential equations of

motion are converted to two sets of first-order ordinary differential equations governing the unknowns that depend only on the radius from the centre of the Earth. One set consists of six equations governing the spheroidal mode of motion (P-SV waves) that is coupled with the gravity field, whereas the other set consists of two equations governing the toroidal mode of motion (SH waves) that is decoupled from the gravity field. Once the frequency-wavelength domain solutions are calculated, the time-space domain solutions can be obtained through summation of the spherical harmonic terms and then the inverse Fourier (Laplace) transform.

For a homogeneous spherical shell, Gilbert and Backus (1968) derived the analytical closed-form solutions for both spheroidal and toroidal modes. However, their analytical spheroidal solutions were obtained under the assumption that the gravity is proportional to the radius, i.e.,  $g(r)/r = \text{const.}$  For a stratified Earth structure, this assumption is only realistic within the core. The complete analytical solutions without the influence of the gravity on the deformation field were presented by Takeuchi and Saito (1972).

Since the gravity effect is significant only for very large wavelengths, i.e., for long-period and low-degree free oscillations, we suggest a hybrid algorithm, in which the long-wavelength spheroidal modes are solved using the numerical Runge-Kutta integration of the equations given in Appendix A, while the small-wavelength spheroidal modes and the complete toroidal modes are solved using the analytical Haskell propagator method.

In the following subsections, we firstly summarize the fundamental toroidal and spheroidal solutions adopted from Takeuchi and Saito (1972). Then, we show the degeneration problems that may arise not only at the static limit but also in the case if the viscoelastic attenuation is considered. One of these degeneration problems (degeneration of the converging pair of spheroidal modes) was solved already by Takeuchi and Saito (1972). We present, for the first time, the solutions for all remaining degeneration problems. Finally, we derived the Haskell propagator for the layered spherical structure in a form similar to that used in the reflectivity method for the layered half-space structure.

## 2.1 Analytical toroidal solutions (SH waves) in a homogeneous spherical shell

The toroidal mode is described by a 2D displacement-stress vector, which is denoted by  $\mathbf{x} = (X_1, rX_2)^T$  in the frequency-wavenumber domain (Appendix A). There are two fundamental toroidal solutions  $(\mathbf{x}_1, \mathbf{x}_2)$  in a homogeneous spherical shell, referred to as the converging and diverging SH waves, which can be expressed in the analytical closed forms (Takeuchi and Saito, 1972),

$$\begin{cases} X_{11} = j_l(x_s), \\ rX_{21} = \mu[(l-1)j_l(x_s) - x_s j_{l+1}(x_s)], \end{cases} \quad (1)$$

and

$$\begin{cases} X_{12} = y_l(x_s), \\ rX_{22} = \mu[(l-1)y_l(x_s) - x_s y_{l+1}(x_s)], \end{cases} \quad (2)$$

respectively, where

$$x_s = k_s r = \frac{\omega}{V_s} r, \quad (3)$$

$\mu$  is the second Lamé constant (also called the shear modulus),  $V_s$  is the S wave velocity,  $\omega$  is the angular frequency,  $r$  is the radius of the spherical shell,  $k_s = \frac{\omega}{V_s}$  is the wavenumber, and  $j_l(x)$  and  $y_l(x)$  are the spherical Bessel functions of degree  $l$  of the first and second kind, respectively.

## 2.2. Analytical spheroidal solutions (P-SV waves) in a homogeneous spherical shell

For deformation of small wavelengths, the gravity effect is negligible. In this case, we consider a hierarchical deformation-gravity coupling, i.e., the gravity depends on the mass redistribution induced by the deformation, but the deformation is decoupled from the gravity. Mathematically, we delete the second and third terms on the right hand side of the first equation of Eq. (A1) in Appendix A, but describe the spheroidal motion still by a 6D displacement-stress vector, which is denoted by  $\mathbf{y} = (rY_1, r^2Y_2, rY_3, r^2Y_4, Y_5, rY_6)^T$  in the frequency-wavenumber domain. Within a homogeneous shell, there are six fundamental

spheroidal solutions  $(\mathbf{y}_1, \mathbf{y}_2, \mathbf{y}_3, \mathbf{y}_4, \mathbf{y}_5, \mathbf{y}_6)$ , which were derived by Takeuchi and Saito (1972).

The first pair of spheroidal solutions, which make up the converging and diverging P waves, respectively, are expressed in the analytical closed forms,

$$\begin{cases} rY_{11} = lj_l(x_p) - x_p j_{l+1}(x_p), \\ r^2 Y_{21} = -(\lambda + 2\mu)x_p^2 j_l(x_p) + 2\mu[l(l-1)j_l(x_p) + 2x_p j_{l+1}(x_p)], \\ rY_{31} = j_l(x_p), \\ r^2 Y_{41} = 2\mu[(l-1)j_l(x_p) - x_p j_{l+1}(x_p)], \\ Y_{51} = 4\pi G\rho j_l(x_p), \\ rY_{61} = 4\pi G\rho(l+1)j_l(x_p), \end{cases} \quad (4)$$

and

$$\begin{cases} rY_{12} = ly_l(x_p) - x_p y_{l+1}(x_p), \\ r^2 Y_{22} = -(\lambda + 2\mu)x_p^2 y_l(x_p) + 2\mu[l(l-1)y_l(x_p) + 2x_p y_{l+1}(x_p)], \\ rY_{32} = y_l(x_p), \\ r^2 Y_{42} = 2\mu[(l-1)y_l(x_p) - x_p y_{l+1}(x_p)], \\ Y_{52} = 4\pi G\rho y_l(x_p), \\ rY_{62} = 4\pi G\rho(l+1)y_l(x_p), \end{cases} \quad (5)$$

where

$$x_p = k_p r = \frac{\omega}{V_p} r, \quad (6)$$

$V_p$  is the P wave velocity,  $\lambda$  is the first Lamé constant,  $\rho$  is the density,  $G$  is the gravitational constant, and  $k_p = \frac{\omega}{V_p}$  is the P wavenumber. The second pair of spheroidal solutions making

up the converging and diverging SV waves are



$$\begin{cases} rY_{13} = -l(l+1)j_l(x_s), \\ r^2Y_{23} = 2\mu l(l+1)[-(l-1)j_l(x_s) + x_s j_{l+1}(x_s)], \\ rY_{33} = -(l+1)j_l(x_s) + x_s j_{l+1}(x_s), \\ r^2Y_{43} = \mu[x_s^2 j_l(x_s) - 2(l^2-1)j_l(x_s) - 2x_s j_{l+1}(x_s)], \\ Y_{53} = 0, \\ rY_{63} = 4\pi G\rho l(l+1)j_l(x_s), \end{cases} \quad (7)$$

and

$$\begin{cases} rY_{14} = -l(l+1)y_l(x_s), \\ r^2Y_{24} = 2\mu l(l+1)[-(l-1)y_l(x_s) + x_s y_{l+1}(x_s)], \\ rY_{34} = -(l+1)y_l(x_s) + x_s y_{l+1}(x_s), \\ r^2Y_{44} = \mu[x_s^2 y_l(x_s) - 2(l^2-1)y_l(x_s) - 2x_s y_{l+1}(x_s)], \\ Y_{54} = 0, \\ rY_{64} = 4\pi G\rho l(l+1)y_l(x_s). \end{cases} \quad (8)$$

The third pair of spheroidal solutions describe the case in which no deformation is caused and the gravity potential is harmonic in the spherical shell. One of these solutions is regular at  $r = 0$ ,

$$\begin{cases} rY_{15} = 0, \\ r^2Y_{25} = 0, \\ rY_{35} = 0, \\ r^2Y_{45} = 0, \\ Y_{55} = r^l, \\ rY_{65} = (2l+1)r^l, \end{cases} \quad (9)$$

and the other is singular at  $r = 0$ ,

$$\begin{cases} rY_{16} = 0, \\ r^2Y_{26} = 0, \\ rY_{36} = 0, \\ r^2Y_{46} = 0, \\ Y_{56} = r^{-(l+1)}, \\ rY_{66} = 0. \end{cases} \quad (10)$$

### 2.3. Underflow, overflow and degeneration at the static limit

At very low frequency ( $\omega \rightarrow 0$ ) or when  $l \gg |x_s| > |x_p|$ , underflow and overflow can arise for numerical computations of the spherical Bessel functions  $j_l(x)$  and  $y_l(x)$ , respectively. In this case, we reformulate the fundamental solutions using the method suggested by Takeuchi and Saito (1972). If  $l > |x_s|^2/2 \geq |x_p|^2/2$ , the two spherical Bessel functions can be replaced by their asymptotic expansion series,

$$\begin{aligned} \phi_l(x) &= \frac{(2l+1)!!}{x^l} j_l(x) \\ &= 1 - \frac{x^2}{2^1(2l+3) \cdot 1!} + \frac{x^4}{2^2(2l+3)(2l+5) \cdot 2!} - \dots, \end{aligned} \quad (11)$$

and

$$\begin{aligned} \varphi_l(x) &= -\frac{x^{l+1}}{(2l-1)!!} y_l(x) \\ &= 1 + \frac{x^2}{2^1(2l-1) \cdot 1!} + \frac{x^4}{2^2(2l-1)(2l-3) \cdot 2!} + \dots, \end{aligned} \quad (12)$$

respectively, where  $n!!$  denotes the semi-factorial of  $n$ , for example,  $(2l+1)!! = 1 \cdot 3 \cdot 5 \cdots (2l+1)$  and  $(2l)!! = 2 \cdot 4 \cdot 6 \cdots (2l)$ . Note that some typos in the Takeuchi and Saito (1972) expression for  $\phi_l(x)$  have been corrected. Accordingly, if  $l > |x_s|^2/2$ , we multiply Eqs. (1) and (2) with the constant factors  $(2l+1)!!/k_s^l$  and  $-k_s^{l+1}/(2l-1)!!$  and obtain

$$\begin{cases} X_{11} = r^l \phi_l(x_s), \\ rX_{21} = r^l \mu \left[ (l-1) \phi_l(x_s) - \frac{x_s^2}{2l+3} \phi_{l+1}(x_s) \right], \end{cases} \quad (1a)$$

and

$$\begin{cases} X_{12} = r^{-(l+1)}\phi_l(x_s), \\ rX_{22} = r^{-(l+1)}\mu[(l-1)\phi_l(x_s) - (2l+1)\phi_{l+1}(x_s)], \end{cases} \quad (2a)$$

respectively. It is interesting to see that in the static case, i.e., when  $\omega = 0$ , the two toroidal solutions are expressed in the following simple form,

$$\begin{cases} X_{11} = r^l, \\ rX_{21} = (l-1)\mu r^l, \end{cases} \quad (1b)$$

and

$$\begin{cases} X_{12} = r^{-(l+1)}, \\ rX_{22} = -(l+2)\mu r^{-(l+1)}, \end{cases} \quad (2b)$$

respectively. These static toroidal solutions are identical with those given by Pollitz (1992).

For the same reason, the spheroidal solutions need to be reformulated at very low frequency or for very large harmonic degrees. For  $l > |x_p|^2/2$ , we can use

$$\begin{cases} rY_{11} = r^l \left[ l\phi_l(x_p) - \frac{x_p^2\phi_{l+1}(x_p)}{(2l+3)} \right], \\ r^2Y_{21} = r^l \left\{ [-(\lambda+2\mu)x_p^2 + 2\mu l(l-1)]\phi_l(x_p) + \frac{4\mu x_p^2\phi_{l+1}(x_p)}{(2l+3)} \right\}, \\ rY_{31} = r^l\phi_l(x_p), \\ r^2Y_{41} = 2\mu r^l \left[ (l-1)\phi_l(x_p) - \frac{x_p^2\phi_{l+1}(x_p)}{(2l+3)} \right], \\ Y_{51} = 4\pi G\rho r^l\phi_l(x_p), \\ rY_{61} = 4\pi G\rho r^l(l+1)\phi_l(x_p), \end{cases} \quad (4a)$$

and

$$\begin{cases}
rY_{12} = r^{-(l+1)} \left[ -(l+1)\varphi_l(x_p) + \frac{x_p^2 \varphi_{l-1}(x_p)}{(2l-1)} \right], \\
r^2 Y_{22} = r^{-(l+1)} \left\{ [-(\lambda+2\mu)x_p^2 + 2\mu(l+1)(l+2)]\varphi_l(x_p) - 4\mu \frac{x_p^2 \varphi_{l-1}(x_p)}{(2l-1)} \right\}, \\
rY_{32} = r^{-(l+1)} \varphi_l(x_p), \\
r^2 Y_{42} = 2\mu r^{-(l+1)} \left[ -(l+2)\varphi_l(x_p) + \frac{x_p^2 \varphi_{l-1}(x_p)}{(2l-1)} \right], \\
Y_{52} = 4\pi G \rho r^{-(l+1)} \varphi_l(x_p), \\
rY_{62} = 4\pi G \rho r^{-(l+1)} (l+1)\varphi_l(x_p),
\end{cases} \quad (5a)$$

in place of Eqs. (4) and (5), respectively.

In principle, Eqs. (7) and (8) for the third and fourth spheroidal solutions in terms of  $x_s$  can be reformulated to the form similar to Eqs. (4a) and (5a), respectively. However, we find that when  $x_p$  and  $x_s \rightarrow 0$ , the third and fourth spheroidal solutions become linearly dependent with the first and second spheroidal solutions, respectively. This kind of degeneration was not considered by Takeuchi and Saito (1972). Here we solve the problem by making the linear combination  $[(4) \cdot (2l+1)!!/k_p^1 + (7) \cdot (2l+1)!!/k_s^1/(l+1) - (9) \cdot 4\pi G \rho] \cdot [-2(2l+3)/k_s^2]$ , resulting in a reformulated spheroidal solution in place of Eq. (7),

$$\begin{cases}
rY_{13} = r^{l+2} [l\eta\delta_l(x_p, x_s) - 2\xi\phi_{l+1}(x_p)], \\
r^2 Y_{23} = 2\mu r^{l+2} [l(l-1)\eta\delta_l(x_p, x_s) - (2l+3)\phi_l(x_p) + 4\xi\phi_{l+1}(x_p) + 2l\phi_{l+1}(x_s)], \\
rY_{33} = r^{l+2} \left[ \eta\delta_l(x_p, x_s) + \frac{2\phi_{l+1}(x_s)}{(l+1)} \right], \\
r^2 Y_{43} = 2\mu r^{l+2} \left[ (l-1)\eta\delta_l(x_p, x_s) - 2\xi\phi_{l+1}(x_p) + \frac{(2l+3)\phi_l(x_s) - 2\phi_{l+1}(x_s)}{(l+1)} \right], \\
Y_{53} = -4\pi G \rho r^{l+2} \xi\beta_l(x_p), \\
rY_{63} = 4\pi G \rho r^{l+2} \{ (l+1)\eta\delta_l(x_p, x_s) - (2l+1)\beta_l(x_s) \},
\end{cases} \quad (7a)$$

where

$$\xi = \left( \frac{V_s}{V_p} \right)^2 = \frac{\mu}{\lambda + 2\mu}, \quad (13)$$

$$\eta = 1 - \xi = \frac{\lambda + \mu}{\lambda + 2\mu}, \quad (14)$$

$$\begin{aligned}\delta_l(x_p, x_s) &= -2(2l+3) \frac{\phi_l(x_p) - \phi_l(x_s)}{x_p^2 - x_s^2} \\ &= 1 - \frac{x_p^2 + x_s^2}{2^1(2l+5) \cdot 2!} + \frac{x_p^4 + x_p^2 x_s^2 + x_s^4}{2^2(2l+5)(2l+7) \cdot 3!} - \dots,\end{aligned}\quad (15)$$

$$\begin{aligned}\beta_l(x) &= -2(2l+3) \frac{\phi_l(x) - 1}{x^2} \\ &= 1 - \frac{x^2}{2^1(2l+5) \cdot 2!} + \frac{x^4}{2^2(2l+5)(2l+7) \cdot 3!} - \dots\end{aligned}\quad (16)$$

Similarly, the fourth spheroidal solution can be reformulated using the linear combination  $[(5) \cdot k_p^{l+1}l/(2l-1)!! - (8) \cdot k_s^{l+1}/(2l-1)!! + (10) \cdot 4\pi G\rho l] \cdot [-2(2l-1)/k_s^2]$ ,

$$\left\{ \begin{aligned} rY_{14} &= r^{-(l-1)} [l(l+1)\eta\varepsilon_l(x_p, x_s) + 2l\xi\varphi_{l-1}(x_p)], \\ r^2Y_{24} &= 2\mu r^{-(l-1)} l [-(l+1)(l+2)\eta\varepsilon_l(x_p, x_s) - (2l-1)\varphi_l(x_p) \\ &\quad - 4\xi\varphi_{l-1}(x_p) + 2(l+1)\varphi_{l-1}(x_s)], \\ rY_{34} &= r^{-(l-1)} [-l\eta\varepsilon_l(x_p, x_s) + 2\varphi_{l-1}(x_s)], \\ r^2Y_{44} &= 2\mu r^{-(l-1)} [l(l+2)\eta\varepsilon_l(x_p, x_s) + 2l\xi\varphi_{l-1}(x_p) \\ &\quad - (2l-1)\varphi_l(x_s) - 2\varphi_{l-1}(x_s)], \\ Y_{54} &= 4\pi G\rho r^{-(l-1)} l\xi\gamma_l(x_p), \\ rY_{64} &= -4\pi G\rho r^{-(l-1)} l(l+1)\eta\varepsilon_l(x_p, x_s), \end{aligned} \right. \quad (8a)$$

where

$$\begin{aligned}\varepsilon_l(x_p, x_s) &= 2(2l-1) \frac{\varphi_l(x_p) - \varphi_l(x_s)}{x_p^2 - x_s^2} \\ &= 1 + \frac{x_p^2 + x_s^2}{2^1(2l-3) \cdot 2!} + \frac{x_p^4 + x_p^2 x_s^2 + x_s^4}{2^2(2l-3)(2l-5) \cdot 3!} + \dots,\end{aligned}\quad (17)$$

$$\begin{aligned}\gamma_l(x) &= 2(2l-1) \frac{\varphi_l(x) - 1}{x^2} \\ &= 1 + \frac{x^2}{2^1(2l-3) \cdot 2!} + \frac{x^4}{2^2(2l-3)(2l-5) \cdot 3!} + \dots,\end{aligned}\quad (18)$$

In the static case, i.e., for  $\omega = 0$ , all functions  $\phi_l$ ,  $\varphi_l$ ,  $\delta_l$ ,  $\beta_l$ ,  $\varepsilon_l$ ,  $\gamma_l$  and  $\sigma_l$ , as defined above, converge to 1. Consequently, all fundamental spheroidal solutions given by Eqs. (4a), (5a), (7a) and (8a) can be expressed in the following closed form,

$$\left\{ \begin{array}{l} rY_{11} = lr^l, \\ r^2Y_{21} = 2\mu l(l-1)r^l, \\ rY_{31} = r^l, \\ r^2Y_{41} = 2\mu(l-1)r^l, \\ Y_{51} = 4\pi G\rho r^l, \\ rY_{61} = 4\pi G\rho(l+1)r^l, \end{array} \right. \quad (4b)$$

$$\left\{ \begin{array}{l} rY_{12} = -(l+1)r^{-(l+1)}, \\ r^2Y_{22} = 2\mu(l+1)(l+2)r^{-(l+1)}, \\ rY_{32} = r^{-(l+1)}, \\ r^2Y_{42} = -2\mu(l+2)r^{-(l+1)}, \\ Y_{52} = 4\pi G\rho r^{-(l+1)}, \\ rY_{62} = 4\pi G\rho(l+1)r^{-(l+1)}, \end{array} \right. \quad (5b)$$

$$\left\{ \begin{array}{l} rY_{13} = [l\eta - 2\xi]r^{l+2}, \\ r^2Y_{23} = 2\mu[l(l-1)\eta + 4\xi - 3]r^{l+2}, \\ rY_{33} = \left[\eta + \frac{2}{l+1}\right]r^{l+2}, \\ r^2Y_{43} = 2\mu\left\{(l-1)\eta - 2\xi + \frac{2l+1}{l+1}\right\}r^{l+2}, \\ Y_{53} = -4\pi G\rho\xi r^{l+2}, \\ rY_{63} = 4\pi G\rho[(l+1)\eta - (2l+1)]r^{l+2}, \end{array} \right. \quad (7b)$$

$$\left\{ \begin{array}{l} rY_{14} = l[(l+1)\eta + 2\xi]r^{-(l-1)}, \\ r^2Y_{24} = 2\mu l[-(l+1)(l+2)\eta - 4\xi + 3]r^{-(l-1)}, \\ rY_{34} = [-l\eta + 2]r^{-(l-1)}, \\ r^2Y_{44} = 2\mu[l(l+2)\eta + 2l\xi - (2l+1)]r^{-(l-1)}, \\ Y_{54} = 4\pi G\rho l\xi r^{-(l-1)}, \\ rY_{64} = -4\pi G\rho l(l+1)\eta r^{-(l-1)}, \end{array} \right. \quad (8b)$$

whereas the fifth and sixth spheroidal solutions given by Eqs. (9) and (10) remain unchanged. The static spheroidal solutions Eqs. (4b), (5b), (7b) and (8b) are consistent with those derived by Pollitz (1992), but they are derived here in an independent way.

#### 2.4. Degeneration caused by viscoelastic attenuation

Within the seismic band, the attenuation of seismic energy caused by the viscoelasticity is usually described through a constant quality factor for each of the P and S waves. Based on the correspondence principle, the viscoelastic dispersion and attenuation can be considered by introducing the complex wave velocities  $V_p$  and  $V_s$  (Kanamori and Anderson, 1977; Müller, 1983),

$$\begin{cases} V_p = V_p^o \left[ 1 + \frac{\ln(f/f_0)}{\pi Q_p} + \frac{i}{2Q_p} \right], \\ V_s = V_s^o \left[ 1 + \frac{\ln(f/f_0)}{\pi Q_s} + \frac{i}{2Q_s} \right], \end{cases} \quad (19)$$

where  $V_p^o$  and  $V_s^o$  are the P and S wave velocity at a reference frequency (e. g., 1 Hz), and  $Q_p$  and  $Q_s$  are the corresponding quality factors, respectively. Thus the arguments  $x_p$  and  $x_s$  take generally complex values, too.

In the case that  $|Im(x)| \gg 1$ , the spherical Bessel functions  $j_l(x)$  and  $y_l(x)$  can become linearly dependent even if  $l$  is not extremely large, implying that the degeneration problem can also be attributed to the viscoelastic attenuation. Consequently, the converging and diverging pairs of the fundamental solutions, i.e., Eqs. (1) and (2), (4) and (5), and (7) and (8), are no longer mutually independent. It seems that this problem can be avoided by using the spherical Hankel functions

$$\begin{cases} h_l^{(1)}(x) = j_l(x) + iy_l(x), \\ h_l^{(2)}(x) = j_l(x) - iy_l(x), \end{cases} \quad (20)$$

instead of the spherical Bessel functions  $j_l(x)$  and  $y_l(x)$ , respectively. However, the same problem arises at the other end, i.e., when  $|x| \rightarrow 0$ . An optimal way is to replace only  $y_l(x)$  in Eqs. (2), (5) and (8) by  $h_n(x)$ , where

$$h_l(x) = \begin{cases} h_l^{(1)}(x), & \text{if } \text{Im}(x) \geq 0, \\ h_l^{(2)}(x), & \text{if } \text{Im}(x) < 0. \end{cases} \quad (21)$$

According to the geophysical convention of forward and inverse Fourier transform, we need to use  $h_l^{(2)}$ .

Up to now, all fundamental solutions for seismic wave propagation in a spherical shell are given in the analytical form and the degeneration problems associated with them in the extreme cases are solved. Based on these results, a propagator algorithm for synthetic seismograms of a layered spherical Earth can be easily formulated in analogy to the reflectivity method for layered half-space models.

## 2.5. Haskell propagator for a layered viscoelastic sphere

If the displacement-stress vector is given by  $\mathbf{y}(r_1)$  at one interface, say  $r_1$ , its value  $\mathbf{y}(r_2)$  at the next interface is related with  $\mathbf{y}(r_1)$  through the Haskell propagator, defined by  $\mathbf{H}(r_2, r_1)$ ,

$$\mathbf{y}(r_2) = \mathbf{H}(r_2, r_1)\mathbf{y}(r_1). \quad (22)$$

As an example, we derive the spherical Haskell propagator for the toroidal mode. In this case,  $\mathbf{H}(r_2, r_1)$  can be expressed in the form,

$$\mathbf{H}(r_2, r_1) = \mathbf{A}(k_s r_2) \cdot \mathbf{A}^{-1}(k_s r_1), \quad (23)$$

where  $\mathbf{A}(x)$  is a  $2 \times 2$  matrix consisting of the fundamental solutions Eqs. (1) and (2) (after  $y_l$  is replaced by  $h_n$ ) as the column vectors,

$$\mathbf{A}(x) = \begin{pmatrix} j_l(x) & h_l(x) \\ \mu[(l-1)j_l(x) - xj_{l+1}(x)] & \mu[(l-1)h_l(x) - xh_{l+1}(x)] \end{pmatrix}. \quad (24)$$

Theoretically both spherical Bessel and Hankel functions in Eq. (24) can be easily calculated using their recursive relations. Practically, however, underflow and overflow can arise because  $j_l(x)$  decreases and  $h_l(x)$  increases exponentially with  $l$  when  $l \gg |x|$ .



Fortunately, in the propagator algorithm we do not need the absolute but relative values of  $j_l(x)$  and  $h_l(x)$  within an arbitrary homogeneous spherical shell from  $r_1$  to  $r_2$ . For this reason, we normalize the left column of matrix  $\mathbf{A}(x)$  by  $[j_l(x) + ixj_{l+1}(x)]$  and the right column by  $h_l(x)$ , and reformulate  $\mathbf{H}(r_2, r_1)$  to

$$\mathbf{H}(r_2, r_1) = \mathbf{B}(k_s r_2) \cdot \mathbf{E}(k_s r_2, k_s r_1) \cdot \mathbf{B}^{-1}(k_s r_1), \quad (25)$$

where

$$\begin{cases} \mathbf{B}(x) = \begin{pmatrix} 1 - z_l^{(j)}(x) & 1 \\ \mu \{ (l-1)[1 - z_l^{(j)}(x)] + iz_l^{(j)}(x) \} & \mu [(l-1) - z_l^{(h)}(x)] \end{pmatrix}, \\ \mathbf{E}(x_2, x_1) = \begin{pmatrix} \exp[w_l^{(j)}(x_2, x_1)] & 0 \\ 0 & \exp[w_l^{(h)}(x_2, x_1)] \end{pmatrix}, \end{cases} \quad (26)$$

and  $z_l^{(j)}(x)$ ,  $z_l^{(h)}(x)$ ,  $w_l^{(j)}(x_2, x_1)$  and  $w_l^{(h)}(x_2, x_1)$  are new functions defined by

$$\begin{cases} z_l^{(j)}(x) = \frac{ixj_{l+1}(x)}{j_l(x) + ixj_{l+1}(x)}, \\ w_l^{(j)}(x_2, x_1) = \ln \frac{j_l(x_2) + ixj_{l+1}(x_2)}{j_l(x_1) + ixj_{l+1}(x_1)}, \\ z_l^{(h)}(x) = \frac{xh_{l+1}(x)}{h_l(x)}, \\ w_l^{(h)}(x_2, x_1) = \ln \frac{h_l(x_2)}{h_l(x_1)}. \end{cases} \quad (27)$$

Note that the choice of the normalization factors  $[j_l(x) + ixj_{l+1}(x)]$  and  $h_l(x)$  is based on the criterion that they never become zero. The reformulated propagator Eq. (25) is fully in analogy to the propagator in the case of a plane Earth model. The new functions defined in Eq. (27) can be calculated using the following recursive relations:

$$\begin{cases} z_l^{(j)}(x) = \frac{ix^2[1 - z_{l+1}^{(j)}(x)]}{(2l+3+ix^2)[1 - z_{l+1}^{(j)}(x)] + iz_{l+1}^{(j)}(x)}, \\ w_l^{(j)}(x_2, x_1) = w_{l-1}^{(j)}(x_2, x_1) - \ln \frac{x_2}{x_1} + \ln \frac{x_2^2 + [1 - x_2^2 + i(2l+1)]z_{l-1}^{(j)}(x_2)}{x_1^2 + [1 - x_1^2 + i(2l+1)]z_{l-1}^{(j)}(x_1)}, \\ z_l^{(h)}(x) = (2l+1) - \frac{x^2}{z_{l-1}^{(h)}(x)}, \\ w_l^{(h)}(x_2, x_1) = w_{l-1}^{(h)}(x_2, x_1) + \ln \frac{x_2}{x_1} + \ln \frac{2l+1 - z_l^{(h)}(x_2)}{2l+1 - z_l^{(h)}(x_1)}. \end{cases} \quad (28)$$

Note that all recursive formulae need to be performed upwards from smaller  $l$  to larger  $l$ , except for the function  $z_l^{(j)}(x)$ , which should be calculated recursively from larger  $l$  to smaller  $l$ . Otherwise, unstable results may arise (Takeuchi and Saito, 1972).

The recursive calculation of  $z_l^{(j)}(x)$  can start at a sufficiently large  $l$ , where an approximation based on Eq. (11) can be used,

$$z_l^{(j)}(x) \sim \frac{x^2}{x^2 - (2l + 3)i}, \quad \text{for } l \gg |x|. \quad (29)$$

For  $l > |x_s|^2/2$ , we design the toroidal propagator using the reformulated fundamental solutions Eqs. (1b) and (2b). In this case, the matrices  $\mathbf{B}(x)$  and  $\mathbf{E}(x_2, x_1)$  are replaced by

$$\begin{cases} \mathbf{B}(x) = \begin{pmatrix} \phi_l(x) & \phi_l(x) \\ \mu \left[ (l-1)\phi_l(x) - \frac{x^2}{2l+3}\phi_{l+1}(x) \right] & \mu[(l-1)\phi_l(x) - (2l+1)\phi_{l+1}(x)] \end{pmatrix}, \\ \mathbf{E}(x_2, x_1) = \begin{pmatrix} \left(\frac{r_2}{r_1}\right)^l & 0 \\ 0 & \left(\frac{r_2}{r_1}\right)^{-(l+1)} \end{pmatrix}. \end{cases} \quad (30)$$

The Haskell propagator associated with the spheroidal solutions can be derived in a similar way. These spherical propagators that we show here for the first time have the same form like those used for a plane Earth model. Therefore, all established methods for numerical efficiency and stability of the half-space propagator algorithm can be adopted simply for the spherical geometry.

### 3. Algorithm

In our hybrid algorithm, a critical frequency  $f_o$  ( $\sim 0.03$  Hz) and a critical harmonic degree  $l_o$  ( $\sim 300$ ) are defined for calculating the spheroidal modes. For  $f \leq f_o$  and  $l \leq l_o$ , the gravity effect is accounted for and the solutions are obtained through the Runge-Kutta integration of the equations described in Appendix A. When  $f > f_o$  or  $l > l_o$ , the gravity effect is neglected and the Haskell propagator algorithm is used. Note that the numerical solutions always differ from the analytical ones. Though such differences might be very small, they may cause a

visible non-physical phase traveling with an apparent velocity determined by  $f_o$  and  $l_o$ . To avoid this artefact, we suggest the use of a certain transition band around  $f_o$  and  $l_o$ , in which both numerical and analytical results are calculated and then combined linearly to ensure a smooth continuity at  $f = f_o$  and  $l = l_o$ . Based on our tests, the artefact can be effectively suppressed by using a transition band around  $f$  and  $l$  of about 20% of  $f_o$  and  $l_o$ , respectively.

The computation procedure can be designed with two loops over the spherical harmonic degree  $l$  and the frequency  $f$ . Since the frequency  $f$  is continuous, the time-domain aliasing problem may be caused by discrete sampling. In comparison, the harmonic degree  $l$  is inherently discrete. However, the space-domain aliasing problem can still be generated by cutting off at the harmonic degree  $l$ , especially if the observation sites are located at the same depth as the source. In addition, the loss-of-precision is well known, which can arise in results obtained from either the Runge-Kutta integration or the Haskell propagator. In the following two subsections, we introduce the methods useful for overcoming the loss-of-precision problem and suppressing the aliasing phases in synthetic seismograms.

### **3.1. The loss-of-precision problem**

According to previous studies, the loss-of-precision problem can be avoided using either the reflectivity method (Fuchs and Müller, 1971; Kennett, 1983) or the second-order minor method (Knopoff, 1964; Dunkin, 1965; Gilbert and Backus, 1966; Kind, 1983; Friederich and Dalkomo, 1995) or the orthonormal propagator method (Wang, 1999; Wang and Kümpel, 2003). Ma et al. (2012) have shown that all these three major methods are based on the same mathematical principle and therefore can solve the numerical problems equally well. In comparison, however, the orthonormal propagator method is the simplest for the implementation and the most efficient for the numerical computation. Therefore, we adopt the orthonormal propagator method in this study.

### **3.2. The time-domain aliasing problem**

Theoretically, the time-domain aliasing problem does not exist if the normal mode method is used. In principle, seismograms can be expanded in terms of the fundamental spheroidal and toroidal modes and their overtones, i.e., the free oscillation spectra. Each fundamental mode or its overtone is represented by a pole in the Laplace plane. The normal mode method is used to locate the poles and characterize them for the amplitude, phase, frequency and quality factor. The normal-mode method is only efficient for synthetic seismograms at very low frequencies ( $\leq 0.15$  Hz). At higher frequencies, the poles become closer to each other leading to inefficiency of their location and instability of their characterization. Consequently, the convergence is slower and the result is less accurate. Therefore, for complete seismograms at higher frequencies (e.g., up to 1-2 Hz) the discrete Fourier transform is more efficient than the normal-mode method.

The time-domain aliasing problem is inherent with the discrete frequency method. If an insufficient frequency sampling rate  $\Delta f = 1/T$  is used, where  $T$  is the length of time window, all seismic phases with the real arrival time beyond the time window will appear in the beginning of the time window. Bouchon (1979) showed that the time-domain aliasing can be effectively suppressed by using the complex frequency technique. In fact, instead of the Fourier spectrum of a seismogram, say  $Y(i\omega)$ , the Laplace spectrum  $Y(\sigma + i\omega)$  can be calculated with the same effort, where  $\sigma$  is a positive constant. The time-domain seismogram  $y(t)$  is then obtained through the Riemann-Mellin integral,

$$\begin{aligned} y(t) &= e^{\sigma t} \int_{-\infty}^{+\infty} Y(\sigma + i\omega) e^{i\omega t} d\omega \\ &= e^{\sigma t} \mathcal{F}^{-1}[Y(\sigma + i\omega)], \end{aligned} \tag{31}$$

where  $\mathcal{F}^{-1}$  represents the inverse Fourier transform. Note that  $Y(\sigma + i\omega)$  is the Fourier spectrum of the function  $e^{-\sigma t}y(t)$ . If the discrete Fourier transform, e.g., FFT (Fast Fourier Transform), is applied to Eq. (31), the time-domain aliasing phases can be suppressed by factor  $e^{-\sigma T}$ . However, the expense for this anti-aliasing technique is a minor loss of the

signal-to-noise ratio at the end of the time window depending on the value chosen for  $\sigma$ . An example is shown in the electronic supplement material to demonstrate how the time-domain aliasing can be suppressed using the complex frequency method (Fig. S1).

### 3.3. The space-domain aliasing problem

The space-domain aliasing appears especially if the observation sites are located at a depth equal or very close to that of the source. In such a case, the spherical harmonic spectra of seismograms are dominated by the near-field terms, which are smooth and converge slowly to zero or are constant with the harmonic degree. The content of regional and teleseismic signals is represented by a small oscillatory part superposed on the large smooth basis. Consequently, any cut-off of the spherical harmonic degree affects the spectral information strongly and results in non-physical wave phases in synthetic seismograms.

The space-domain aliasing can be suppressed in a similar way as for the time-domain aliasing. Assume that

$$y(\theta) = \sum_{l=m}^{\infty} F_l P_l^m(\cos\theta), (m \geq 0), \quad (32)$$

where  $\theta$  is the angular epicentral distance, and  $P_l^m(x)$  are the associated Legendre polynomials of degree  $l$  and order  $m$ . Wang and Wang (2007) showed that the function  $y(\theta)$  can be expressed equivalently by

$$y(\theta) = \frac{1}{2\sin^2(\frac{\theta}{2})} \sum_{l=m}^{\infty} G_l P_l^m(\cos\theta), (m \geq 0), \quad (33)$$

where  $G_l$  represents the Legendre spectrum of the function  $2\sin^2(\theta/2) \cdot y(\theta)$  and is related to  $F_l$  by

$$G_l = \begin{cases} F_l - \frac{l+m+1}{2l+3} F_{l+1}, & l = m, \\ F_l - \frac{l+m+1}{2l+3} F_{l+1} - \frac{l-m}{2l-3} F_{l-1}, & l > m. \end{cases} \quad (34)$$

Note that for large  $l$ ,  $G_l \sim F_l - (F_{l+1} + F_{l-1})/2 = -\Delta^2 F_l/2$ , where  $\Delta^2$  represents the second-order finite difference operator. Therefore, Eq. (34) is called the differential transform (Wang and Wang, 2007). For observation sites in the far field, the necessary cut-off harmonic degree for calculating  $y(\theta)$  can be considerably reduced by using Eq. (33) instead of (32). As shown in Wang and Wang (2007), sometimes it is even necessary to use a higher-order differential transform depending on where and how sharp the user wants to cut off the harmonic spectrum. An application example of the differential transform is shown in the electronic supplement material (Figs. S2-3).

### 3.4. Implementation of the code QSSP

In our QSSP code, a large earthquake is represented by a number of point sources and synthetic seismograms are calculated in two steps. First, for a given depth level of seismic stations, a database of spectral Green's functions for discrete source depths is created, which can then be used repeatedly to synthesize seismograms for any earthquake described with a finite-fault kinematic source model. With personal PCs nowadays, the maximum harmonic degree can be defined as large as 25,000. If the complete waveform is desired, the frequency range can cover from 0 to 2 Hz or higher at the global scale. The discrete point sources can be represented as double-couples or as full moment tensors. They can be placed in any layer in the solid Earth, but also in the oceanic or atmospheric layers. Earth models used can include optionally the solid inner core, the liquid outer core, the mantle, the ocean and the atmosphere, each of which can have a multi-layered structure. All computations are carried out using a single code and controlled with a self-explanatory input file.

## 4. Tests

In this section, we show several computation tests of the QSSP code. In Test 1, teleseismic synthetic seismograms are calculated and compared with those obtained by the reflectivity code, revealing the Earth curvature effect. Test 2 demonstrates the gravity effect on long-period Rayleigh waves and free oscillations. In Test 3, tsunami and infrasound waves excited

by the 2004 Mw9.3 Sumatra earthquake are simulated. Test 4 shows a near-field displacement seismogram with static offset calculated for the 2011 Mw8.8 Maule earthquake in comparison with the high-rate GPS data. Finally, Test 5 shows a cross check between QSSP and the code PSGRN/PSCMP (Wang et al., 2006) for a static dislocation model. Additional examples are provided in the electronic supplement material.

#### **4.1. The Earth curvature effect at teleseismic distances - comparison with the reflectivity code**

So far complete synthetic seismograms are computed by the widely used reflectivity code based on a layered half-space model, in which the Earth curvature effect is considered approximately through an earth-flattening transformation (EFT) developed by Müller (1977). Using the EFT, body waves observed at the surface of a spherical model can be simulated using a properly stratified half-space model. The EFT formulae were validated originally only for a homogeneous sphere. It is interesting to see how well the EFT works for a realistic Earth model. For this purpose, we use the seismic reference model AK135 (Kennett et al., 1995) and compare complete synthetic seismograms for very large distances calculated by the reflectivity code QSEIS implemented based on Wang (1999) and the code QSSP developed in the present study, respectively. Velocity seismograms are calculated for an explosion source in 230 km depth and for arrivals before the pS phase (Fig. 1). At distances within about  $140^\circ$ , most body waves based on the two models agree with each other not only for the arrival time but also for the waveform and amplitude. Large differences are found for surface waves and few complicated multiple waves as well. In particular, the EFT fails for distances close to  $180^\circ$  and waves that exist only due to the spherical geometry, such as e.g., the P'P' (PKPPKP) phase, cannot be produced using a plane Earth model. The arrivals of multi-pathing rays through the outer and inner core lead to significant high-frequency energy at large epicentral distances and late times (e.g.,  $>1200$  s at  $120^\circ$ ), which are not modelled by flat-earth reflectivity codes. Therefore, QSSP has a potential for improving studies on the structure and

attenuation of the outer and inner core from multiple pathing body (e.g., Ivan and Wang, 2013) and surface waves. Note that the results shown in Fig. 1 also provide a cross validation between the two independent codes QSEIS (Wang, 1999) and QSSP. More examples for calculating multiple core phases like PmKP ( $m \leq 10$ ) are shown in the electronic supplement material (Figs. S4-7).

#### 4.2. The gravity effect on long-period Rayleigh waves and free oscillations

In this test a long time window of 12 hours is chosen to include Rayleigh waves circling several times around the Earth. Figure 2 shows synthetic seismograms of the vertical component at the distance of  $90^\circ$  for a strike-slip source at the depth of 33 km. To demonstrate the gravity effect, the synthetics are calculated by switching on and off the gravity-deformation coupling in the hybrid algorithm, i.e., by selecting  $f_o/l_o = 0.03 \text{ Hz}/300$  and  $0.0 \text{ Hz}/0$ , respectively. As expected, the gravity effect is significant only for very long-period Rayleigh waves and late arriving global Rayleigh wave groups. At periods of a few minutes or longer, the Earth gravity may delay the arrival time by about a half period and modify the waveform considerably. Analysis of such wave trains, as e.g. the moment tensor inversion from long period surface waves for mega-thrust earthquakes, may be biased if the gravity effect is not properly considered. Note that gravity can also affect the W-phase leaky mode, which is nowadays used for fast moment tensor inversion, although the effect is much smaller there (see Fig. S8 in the electronic supplement material).

Next we calculate the free oscillation spectra caused by the 2004 Mw9.3 Sumatra earthquake. For simplicity, the earthquake source is simplified by a point thrust (dip =  $8^\circ$ ) dislocation at the depth of 30 km. Figure 3 shows the Fourier amplitude spectra of the spherical harmonic terms of degree 0, 1 and 2. The spheroidal and toroidal modes are denoted by  ${}_nS_l$  and  ${}_nT_l$ , respectively. Their fundamental frequencies ( $n = 0$ ) and overtones ( $n \geq 1$ ) are clearly identified by the amplitude peaks. Note that the toroidal modes  ${}_nT_0$  are meaningless per definition. The fundamental modes  ${}_0S_1$  and  ${}_0T_1$  are missing because they



would mean a translational motion of the mass centre of the Earth and a rigid rotation of the Earth, respectively, which can never be excited by any internal force like earthquakes. The gravity effect on  ${}_0S_0$  is the most significant, causing a decrease of the frequency by 0.1249 mHz or 13.30%.

The spheroidal mode  ${}_1S_1$  is characterized by the translational oscillation of the inner solid core. Because of the Earth's rotation and elliptical figure, there exist the axial, prograde and retrograde modes of  ${}_1S_1$ , which are known as the Slichter triplet (Slichter, 1961). The splitting is dominantly caused by the Coriolis force due to the Earth's rotation (Dahlen, 1968; Dahlen and Tromp, 1998). In particular, the retrograde mode has the largest frequency (shortest period) of the triplet because the Coriolis force enhances the elasto-gravitational feedback, and vice versa for the prograde mode. It is known that the frequency of the Slichter mode is strongly dependent on the density contrast between the inner and outer core. The smaller the density contrast, the longer the period. Therefore, the observation of the Slichter mode would provide a useful constraint on the inner and outer core structure. So far, there have been many claims of observation of the Slichter triplet mostly based on the records of superconducting gravimeters, good evidence is still lacking (see e.g., Hinderer et al.; 1995; Ochi et al., 2000; Rosat et al., 2006; Ding and Chao, 2015).

Figure 4 shows the power spectrum around  ${}_1S_1$ , whose degenerate frequency (period) and Q value are determined at 51.1824  $\mu$ Hz (5.4272 h) and 6,060 for the PREM model (Dziewanski and Anderson, 1981), respectively. The very large Q value results from the nearly inviscid fluid outer core used in the model. Our estimate of the degenerate period agrees well with the recent results (5.219 – 5.420 h) obtained by different authors based on the same Earth model PREM (Crossley, 1993; Rochester and Peng, 1993; Peng, 1997; Rogister, 2003), but it is significantly larger than those (4.309 – 4.600 h) based on the Earth model 1066A (Dahlen and Sailor, 1979; Crossley et al., 1992; Crossley, 1993; Rieutord, 2002; Rogister, 2003). The peak displacement amplitude of  ${}_1S_1$  caused by the 2004 Mw9.3 Sumatra earthquake are

estimated to be 0.27  $\mu\text{m}$  on the surface and 0.29 mm in the inner core if the earthquake source is simplified by a point dislocation ( $M_w = 9.3$ , strike =  $329^\circ$ , dip =  $8^\circ$ , rake =  $110^\circ$ , latitude =  $3.09^\circ$ , longitude =  $94.26^\circ$  and depth = 30 km). Correspondingly, the maximum gravity change on the surface is in the order of 0.1 nGal (including both inertial and free-air effects, as could be measured by a gravimeter). If the finite-fault source model derived from the near-field GPS data (Hoechner et al., 2008) is used, however, the amplitudes of the three observables are increased to 0.79  $\mu\text{m}$ , 0.83 mm and 0.25 nGal, respectively. Note that the free-air gradient of the surface gravity is 0.30827 nGal/ $\mu\text{m}$ . Therefore, the 0.25 nGal gravity change results almost from the free-air effect. The inertial part and the part due to the mass redistribution are together only about 0.5% of the free-air effect, i.e., 1.25 nGal, for the Slichter mode.

If the rotational and elliptical splitting is considered, the Slichter triplet frequencies of the PREM model can be derived from its degenerate frequency based on the perturbation theory. Using the formulae by Dahlen (1968) and Dahlen and Sailor (1979), which include a slight shift in addition to the splitting, we obtain 51.918  $\mu\text{Hz}$  (5.350 h), 45.948  $\mu\text{Hz}$  (6.045 h) and 57.831  $\mu\text{Hz}$  (4.803 h) for the axial, prograde and retrograde modes, respectively. Correspondingly, the global gravity change caused by the Slichter triplet, as it could be measured by gravimeters on the Earth's surface, can be expressed in the form

$$\Delta g(\theta, \varphi, t) = A_a \cos(\theta) \cos(\omega_a t + \delta_a) + \sin(\theta) [A_p \cos(\omega_p t - \varphi + \delta_p) + A_r \cos(\omega_r t + \varphi + \delta_r)], \quad (35)$$

where  $\theta$  is the co-latitude,  $\varphi$  is the longitude, the indices  $(a, p, r)$  denote the axial, prograde and retrograde modes, and  $(A, \omega, \delta)$  are their amplitude, frequency and initial phase, respectively. We may assume that the amplitudes and initial phases of the Slichter triplet are not significantly influenced by the Earth's rotation like their frequencies. By calculating the frequency-domain resonance responses (before the inverse Fourier transform) at three different locations on the Earth's surface, we are able to estimate the amplitudes and phases of

the Slichter triplet excited by the 2004 great Sumatra earthquake without taking into account for the effect of the Earth's rotation. Using the finite-fault source and the PREM model, we obtain that  $(A_a, \delta_a) = (0.032 \text{ nGal}, 175^\circ)$ ,  $(A_p, \delta_p) = (0.125 \text{ nGal}, 269^\circ)$  and  $(A_r, \delta_r) = (0.125 \text{ nGal}, 83^\circ)$ . These results indicate that in the present case the Slichter mode is dominated by the motion within the equatorial plane because of the near-equator location of the exciting source. Furthermore, the equal amplitude of the prograde and retrograde modes means that the inner core oscillates in principle like a Foucault pendulum. However, in contrast to the Foucault pendulum the prograde and retrograde Slichter singlets are also influenced by the elasticity of the Earth (particularly of the outer core). The splitting is therefore not only defined by the Coriolis force but also by the elastic forces. The induced gravity change starts with its negative peak value of about  $-0.25 \text{ nGal}$  in the epicentral area and positive peak value of  $+0.25 \text{ nGal}$  at the antipodal area of the earthquake. The peak to peak amplitude around the equator in the postseismic period may reach about  $0.5 \text{ nGal}$ , which is more than twice as large as that estimated using the point source approximation, but still orders of magnitude smaller than what can be resolved by a modern superconducting gravimeter, explaining how challenging would be the observations of the Slichter modes if they are excited seismically.

Complete normal modes in the low frequency band of up to  $2.0 \text{ mHz}$  are shown in the electronic supplement material (Tab. S1). For the same Earth model (the isotropic version of PREM), the eigenfrequencies calculated by QSSP agree excellently with those by MINEOS ( $< 0.04\%$ ), but the  $Q$  values given by QSSP are systematically smaller than those by MINEOS (maximum of  $11\%$  for  ${}_0S_0$ ). We explain the large discrepancy in the  $Q$  values by the approximation approach used in MINEOS to determine the attenuation effect. Actually, MINEOS calculates the normal modes in two steps. First the eigenfrequency and eigenfunction are determined for a purely elastic Earth model without attenuation. Then the quality factor (equivalent to the imaginary part of eigenfrequency) and its effect on the eigenfrequency are estimated using the first-

order perturbation method. In contrast, QSSP determines the eigenfrequency and quality factor simultaneously using the correspondence principle without any approximation.

### 4.3. Tsunami and infrasound waves

In this test, synthetic seismograms for tsunami and infrasound waves caused by the 2004 Mw9.3 Sumatra earthquake are computed with the code QSSP. The Earth model used is the PREM model, which includes 3 km ocean layer, combined with a standard atmosphere up to 86 km height (US Standard Atmosphere: US Government Printing Office, Washington, DC, 1976). We calculate the pressure changes along a southward profile from the epicentral distance of  $10^\circ$  to  $70^\circ$  using a realistic earthquake source model, which consists of 432 sub-faults with the slip distribution adopted from Hoechner et al. (2008). The results are shown in Fig. 5. At the ocean bottom, Rayleigh waves and tsunami waves are visible. The latter propagate with a velocity of about 170 m/s, consistent with the ocean depth of 3 km. At the ocean surface, acoustic-infrasound gravity waves are visible additionally, which propagate through the atmosphere with the velocity smaller than 340 m/s (the near-ground sound speed). The acoustic-infrasound waves are missing (insignificant) at the ocean bottom because of the isostatic equilibrium. It is interesting to see that the tsunami wave can cause the pressure changes not only at the ocean bottom but also at the ocean surface and the tsunami waveforms observed at the two different levels have the opposite polarization. The reason is that for any water level change of  $\Delta h$ , the pressure change is  $\rho_w g \Delta h$  if it is measured by a sensor fixed at the ocean bottom, but  $-\rho_a g \Delta h$  if it is measured by a sensor swimming on the water surface, where  $\rho_w$  and  $\rho_a$  are the densities of water and air, respectively. The complicated infrasound and tsunami waveforms shown in Fig. 5 are not only related to the near-field ocean bottom motion calculated using the kinematic finite-fault source model, which extends about 1000 km and lasted about 10 minutes, but also to the reverberation effect within the ocean layer.

Like the solid Earth, the atmosphere and the ocean can exhibit their own free oscillations, which are made through interference of infrasound and tsunami waves cycling

around the Earth, respectively. Using the normal mode method, Lognonné et al. (1998) investigated the coupling between the solid Earth and atmosphere but without a global ocean. For convenience, we denote the atmospheric free oscillation modes by  ${}_nA_l$  and the oceanic ones by  ${}_nW_l$ , in analogy to  ${}_nS_l$  or  ${}_nT_l$  for the solid Earth free oscillations. To study  ${}_nA_l$ , we combine the US Standard Atmosphere model with a modified Earth model PREM (with 3 km frozen ocean) and calculate the Fourier spectra of synthetic infrasound seismograms. The results are shown in the upper panel of Fig. 6, where the long-period fundamental modes  ${}_0A_l$  for  $l > 0$  are clearly identified by the Fourier amplitude peaks. The longest atmospheric free oscillation period is given by  ${}_0A_1$ , which is estimated to be 27.4 h for the US standard model.  ${}_0A_0$  and  ${}_nA_l$  for  $n > 0$  are beyond the plotted frequency band. Similarly, the long-period fundamental modes  ${}_0W_l$  for  $l > 0$  are shown in the lower panel of Fig. 6, which are calculated based on the original PREM with 3 km ocean layer. The longest oceanic free oscillation period belongs to  ${}_0W_1$  and is 52.8 h for the PREM model.

Modelling and source inversion studies, which aim to combine seismic and oceanic layer pressure recordings, can benefit from an all-in-one code like QSSP which considers the full coupling of these waves. For instance, QSSP was used by Heimann et al. (2013) to estimate the source parameters of the 2013 Cheliabinsk meteorite explosion from seismic, long period Rayleigh waves, and by Raveloson et al. (2012) for interpreting the tsunami and acoustic-gravity signals of the 2004 Indian Ocean tsunami recorded by the IMS infrasound arrays.

#### **4.4. Near-field displacement seismograms with permanent offset**

This test demonstrates the complete synthetic seismograms for the near-field displacement. As an example, the 2010 Mw8.8 Maule (Chile) earthquake is considered. The fault slip model is adopted from Tong et al. (2010), derived from the InSAR and GPS data. This source model includes 1338 sub-faults of the uniform size of 10 km. For simplicity, the kinematic rupture process is simulated using a uniform rupture propagation velocity of 2.65 km/s and the

Brune's source time function with a uniform characteristic rise time of 1.5 s. Figure 7 shows the synthetic displacement seismograms at Station ROBL ( $-32.9760^{\circ}\text{N}$ ,  $-71.0157^{\circ}\text{E}$ ), compared with the high-rate (1 sps) GPS data (Christophe Vigny, pers. communication, 2011).

Note that there is a significant discrepancy between the vertical static offsets of the high-rate GPS data and the daily GPS data. As expected, the synthetic static offsets agree better with the daily GPS data, based on which the slip model was derived. The displacement time histories are not well reproduced like the static offsets, possibly because of the use of the simplified rupture-time and rise-time distributions, but also the neglecting of the non-global ocean effect. A possible contribution of QSSP is seen for the simultaneous inversion of high rate continuous GPS together with near field accelerometer and regional broadband seismic data, e.g. to estimate the time dependent slip distribution of earthquakes. The advantage of QSSP is that all modelled Green's functions are based on the same method and the same Earth model parametrization.

#### **4.5. Static deformation field and gravity changes near the earthquake fault**

Here we demonstrate a cross check between QSSP and PSGRN/PSCMP (Wang et al., 2006) for calculating near-field static deformation and gravity changes caused by the 2007 Mw7.7 Tocopilla (Chile) earthquake. A finite-fault source model is used, which consists of about 1000 fault patches adopted from Motagh et al. (2010). Comparisons of the 3-component surface displacement and gravity changes calculated using QSSP and PSGRN/PSCMP are shown in Figs. 8 and 9, respectively. The differences between the results from the two independent codes are on the level of a few percent that is about within the expected numerical accuracy. It should be noted that PSGRN/PSCMP is based on a half-space geometry and the gravity effect is accounted for using the so-called Wang approach (Segall, 2010). The good agreements shown in Figs. 8 and 9 validate each other's performances of the two independent tools. Thus, QSSP can be beneficial for a joint inversion of InSAR derived static near-field displacements with teleseismic broadband seismograms using a consistent

method and Earth model parametrization. Additionally, QSSP helps to understand the complete gravity effect of dislocation sources, which is affected by the displacement of the free surface and the internal layer interfaces, but also by the elastic deformation of the continuum.

## 5. Discussion and conclusions

We present a hybrid method for stable and efficient computations of complete synthetic seismograms based on a spherically symmetric and self-gravitating Earth model with a typical structure of the atmosphere, ocean, mantle, liquid core and solid core. For large wavelengths, a numerical scheme is used to solve the geodynamic boundary-value problem without any approximation on the deformation and gravity coupling. With the decreasing wavelength, the gravity effect on the deformation becomes negligible and the analytical propagator scheme can be used. In particular, we propose the useful approaches to overcome the degeneration problems, which may arise when using the analytical solutions, and the loss-of-precision problems which may arise in both analytical and numerical schemes.

Based on the hybrid method, an all-in-one code QSSP was implemented, which can be used for simulating body waves, surface waves, tsunami waves, infrasound gravity waves, free oscillations, and near-field static deformation caused by earthquakes. On a modern personal PC, complete synthetic seismograms can be easily calculated at the global scale for frequencies of up to 2 Hz. By using a narrow slowness window, body wave seismograms of even higher frequency (up to 5 Hz) can be simulated, too.

The performance of the code QSSP is demonstrated by various tests. One interesting test is to estimate the free oscillation mode  ${}_1S_1$ , which is known as the Slichter mode, based on the Earth model PREM. It is found that if the Slichter mode could be caused by the 2004 Mw9.3 Sumatra earthquake, its maximum amplitude for the gravity change on the Earth surface is about a quarter of one nGal that is at least one order smaller than what can be resolved by a modern superconducting gravimeter. In another test, tsunami and infrasound

waves and the atmospheric and oceanic free oscillations are simulated. It should be emphasized that these simulations are based on spherically symmetric and non-rotating Earth models. In practice, the laterally heterogeneous bathymetry, wind and the effect of the Coriolis force make it difficult to observe the individual free oscillation modes of the real atmosphere and ocean. Nevertheless, the results from such simulations are helpful for understanding the physical basis for the mechanical (gravitational) coupling between the different subsystems of the Earth.

QSSP is useful for the study of long period surface waves as well as for high-frequency body waves which travel through the outer and inner core and experience multiple reflections and scattering in the Earth. It is also useful for various kinds of source studies, from point source moment tensor inversion to slip imaging on the rupture plane of major earthquakes, especially if different types of seismic, geodetic, oceanic and engineering data are inverted simultaneously. The original QSSP as a stand-alone FORTRAN code can be downloaded from <ftp://ftp.gfz-potsdam.de/pub/home/turk/wang/>. The source inversion problem is supported by means of global and regional pre-calculated Green's function databases based on QSSP, which are provided as a community service at (<http://kinherd.org/>) or can be calculated individually using the Python toolbox Fomosto (<http://pyrocko.org/>). On the other hand, the high-precision results of QSSP can provide an ideal reference for global 3D modelling using, e.g., the spectral-element method (Komatitsch and Tromp, 1999).

In summary, the advantage of the all-in-one code QSSP is the use of a uniform algorithm based on a solid and well established theory. Therefore, bugs can be easily detected and modelling errors can be minimized. Additionally, with a small extension the QSSP can be used for modelling viscoelastic post-seismic deformation or postglacial rebound problems. The corresponding stand-alone FORTRAN code (QSSPSTATIC) is free available on the web, too.



## **Acknowledgements**

The basic theory, approach and code of QSSP were developed over more than one decade by the first author alone. The co-authors contributed in terms of theory and code verification and testing, improvements, implementation of interfaces, examples and manuscript preparation. However, many other scientists and students who worked with QSSP have helped by providing feedback or formulating requests for further consideration. The authors thank Walter Zürn and another anonymous reviewer for their valuable comments.

## Appendix A. Description of the geodynamic boundary-value problem based on a spherically symmetric, isotropic linear elastic and self-gravitating Earth model

Assume an infinitesimal dynamic deformation process superposed on the initial hydrostatic equilibrium of a spherically symmetric, elastic and self-gravitating Earth. Using the spherical co-ordinate system  $(r, \theta, \varphi)$  with the origin ( $r = 0$ ) at the Earth mass centre, the frequency-domain equations of motion governing the infinitesimal deformation is written in the form,

$$\begin{cases} -\rho\omega^2\mathbf{u} = \nabla \cdot \boldsymbol{\sigma} + \rho\nabla(\psi - gu_r) + \rho g(\nabla \cdot \mathbf{u})\mathbf{e}_r + \mathbf{f}, \\ \nabla^2\psi = 4\pi G\nabla \cdot (\rho\mathbf{u}), \end{cases} \quad (\text{A1})$$

(see, e.g., Dahlen, 1972), where  $\omega$  is the angular frequency,  $\rho = \rho(r)$  is the density,  $G$  is the gravitational constant,  $\mathbf{f} = \mathbf{f}(r, \theta, \varphi)$  is the body force (seismic source),  $\mathbf{u} = \mathbf{u}(r, \theta, \varphi)$  is the particle displacement vector,  $\psi = \psi(r, \theta, \varphi)$  is the incremental gravity potential,  $\boldsymbol{\sigma} = \boldsymbol{\sigma}(r, \theta, \varphi)$  is the incremental stress tensor, and  $g = g(r)$  is the Earth gravity (downwards positive),

$$g(r) = \frac{4\pi G}{r^2} \int_0^r \rho(\xi)\xi^2 d\xi. \quad (\text{A2})$$

For the interested reader, we notice that in the above equations,  $\boldsymbol{\sigma}$  is the incremental stress tensor in the Lagrangian (or material) description, whereas  $\psi$  is the incremental gravity potential in the Eulerian (or spatial) description. The choice of this mixed description is for the reason that the constitutive law relating the stress to strain is material based, but the local gravity potential is commonly used in the space geodesy. Additionally, the mixed description leads to a simple form of the boundary conditions (Wang, 1997).

For the isotropic, linear elastic medium, the stress tensor is related to the strain tensor by Hooke's law,

$$\boldsymbol{\sigma} = \lambda(\nabla \cdot \mathbf{u})\mathbf{I} + \mu[\nabla\mathbf{u} + (\nabla\mathbf{u})^T], \quad (\text{A3})$$

where  $\mathbf{I}$  is the unit tensor, and  $\lambda = \lambda(r)$  and  $\mu = \mu(r)$  are the two Lamé constants.

At an interior interface  $r = r_i$ , the displacement, stress and potential satisfy in general the following continuity conditions,

$$\begin{cases} \mathbf{u}|_{\pm}^{\pm} = \mathbf{0}, \\ \mathbf{e}_r \cdot \boldsymbol{\sigma}|_{\pm}^{\pm} = \mathbf{0}, \\ \psi|_{\pm}^{\pm} = 0, \\ \mathbf{e}_r \cdot (\nabla\psi - 4\pi G\rho\mathbf{u})|_{\pm}^{\pm} = 0, \end{cases} \quad (A4)$$

where  $\mathbf{u}|_{\pm}^{\pm} = \mathbf{u}(r_i^+, \theta, \varphi) - \mathbf{u}(r_i^-, \theta, \varphi)$  denotes the jump of displacement through the interface, and so on. If the interface is frictionless, for example, at the boundary between the core and mantle or between the inner core and outer core, the displacement continuity is required only for its normal component, i.e.,  $\mathbf{u}|_{\pm}^{\pm} = \mathbf{0}$  is replaced by  $u_r|_{\pm}^{\pm} = 0$  in this case. At the Earth centre, the regularity conditions are required,

$$\begin{cases} \mathbf{u}|_{r \rightarrow 0} < \infty, \\ \mathbf{e}_r \cdot \nabla\psi|_{r \rightarrow 0} < \infty. \end{cases} \quad (A5)$$

The free surface conditions are expressed by

$$\begin{cases} \mathbf{e}_r \cdot \boldsymbol{\sigma}|_{r=a} = \mathbf{0}, \\ \mathbf{e}_r \cdot (\nabla\psi - 4\pi G\rho\mathbf{u})|_{r=a} = 0. \end{cases} \quad (A6)$$

where  $a$  is the Earth radius, and in the mass-free external space, the potential is required to be harmonic.

In the spectral method, the frequency-domain field quantities are expanded in terms of vector spherical harmonics,

$$\begin{cases} \mathbf{u} = \sum_{l=0}^{\infty} \sum_{m=-l}^l [U_l^m(r) \mathbf{R}_l^m(\theta, \varphi) + V_l^m(r) \mathbf{S}_l^m(\theta, \varphi) + W_l^m(r) \mathbf{T}_l^m(\theta, \varphi)], \\ \psi = \sum_{l=0}^{\infty} \sum_{m=-l}^l \Phi_l^m(r) Y_l^m(\theta, \varphi), \\ \mathbf{e}_r \cdot \boldsymbol{\sigma} = \sum_{l=0}^{\infty} \sum_{m=-l}^l [E_l^m(r) \mathbf{R}_l^m(\theta, \varphi) + F_l^m(r) \mathbf{S}_l^m(\theta, \varphi) + G_l^m(r) \mathbf{T}_l^m(\theta, \varphi)], \end{cases} \quad (A7)$$

where

$$\begin{cases} \mathbf{R}_l^m(\theta, \varphi) = \mathbf{e}_r Y_l^m(\theta, \varphi), \\ \mathbf{S}_l^m(\theta, \varphi) = \mathbf{e}_\theta \frac{\partial}{\partial \theta} Y_l^m(\theta, \varphi) + \mathbf{e}_\varphi \frac{1}{\sin \theta} \frac{\partial}{\partial \varphi} Y_l^m(\theta, \varphi), \\ \mathbf{T}_l^m(\theta, \varphi) = \mathbf{e}_\theta \frac{1}{\sin \theta} \frac{\partial}{\partial \varphi} Y_l^m(\theta, \varphi) - \mathbf{e}_\varphi \frac{\partial}{\partial \theta} Y_l^m(\theta, \varphi), \end{cases} \quad (A8)$$

and

$$Y_l^m(\theta, \varphi) = P_l^{|m|}(\cos \theta) e^{im\varphi}, \quad (A9)$$

are the spherical surface functions and  $P_l^{|m|}(\cos \theta)$  the associated Legendre polynomials of degree  $l$  and order  $m$ . Note that, if synthetic Green's functions are calculated for typical seismic sources, that is, a single force or a point dislocation,  $|m|$  only takes 0, 1 and 2.

Using the completeness and orthogonality of the spherical surface functions, the partial differential equations of motion Eq. (A1) can be converted to a system of ordinary differential equations governing the expansion coefficients in Eq. (A7). Thus, the toroidal mode is described by a generalized 2D displacement-stress vector,

$$\mathbf{X} = (W_l^m, G_l^m)^T, \quad (A10)$$

and the spheroidal mode by a generalized 6D displacement-stress vector,

$$\mathbf{Y} = \left( U_l^m, E_l^m, V_l^m, F_l^m, \Phi_l^m, \dot{\Phi}_l^m + \frac{l+1}{r} \Phi_l^m - 4\pi G \rho U_l^m \right)^T, \quad (A11)$$

where the dot denotes the derivative with respect to  $r$ .

In the case of the spherical symmetry, the two different modes are decoupled from each other and therefore can be solved independently. The ordinary differential equations of motion governing the toroidal mode is given by

$$\begin{cases} \dot{X}_1 = \frac{1}{r} X_1 + \frac{1}{\mu} X_2, \\ \dot{X}_2 = \left[ -\rho \omega^2 + \frac{(l-1)(l+2)\mu}{r^2} \right] X_1 - \frac{3}{r} X_2. \end{cases} \quad (A12)$$

For a homogeneous spherical shell, Eq. (A12) can be solved analytically. There exist two fundamental toroidal solutions, which are given in the main text.

The ordinary differential equations of motion governing the spheroidal mode is given by

$$\begin{cases}
 \dot{Y}_1 = -\frac{2\lambda}{(\lambda+2\mu)r}Y_1 + \frac{1}{\lambda+2\mu}Y_2 + \frac{l(l+1)\lambda}{(\lambda+2\mu)r}Y_3, \\
 \dot{Y}_2 = \left[-\rho\omega^2 - \frac{4\rho g}{r} + \frac{4\mu(3\lambda+2\mu)}{(\lambda+2\mu)r^2}\right]Y_1 - \frac{4\mu}{(\lambda+2\mu)r}Y_2 \\
 \quad + l(l+1)\left[\frac{\rho g}{r} - \frac{2\mu(3\lambda+2\mu)}{(\lambda+2\mu)r^2}\right]Y_3 + \frac{l(l+1)}{r}Y_4 + \frac{(l+1)\rho}{r}Y_5 - \rho Y_6, \\
 \dot{Y}_3 = -\frac{1}{r}Y_1 + \frac{1}{r}Y_3 + \frac{1}{\mu}Y_4, \\
 \dot{Y}_4 = \left[\frac{\rho g}{r} - \frac{2\mu(3\lambda+2\mu)}{(\lambda+2\mu)r^2}\right]Y_1 - \frac{\lambda}{(\lambda+2\mu)r}Y_2 \\
 \quad + \left\{-\rho\omega^2 + \frac{2\mu}{r^2}\left[\frac{2l(l+1)(\lambda+\mu)}{\lambda+2\mu} - 1\right]\right\}Y_3 - \frac{3}{r}Y_4 - \frac{\rho}{r}Y_5, \\
 \dot{Y}_5 = 4\pi G\rho Y_1 - \frac{l+1}{r}Y_5 + Y_6, \\
 \dot{Y}_6 = \frac{4\pi G\rho(l+1)}{r}Y_1 - \frac{4\pi G\rho l(l+1)}{r}Y_3 + \frac{l-1}{r}Y_6.
 \end{cases} \tag{A13}$$

Note that due to the spherical symmetry, the harmonic order  $m$  does not appear in the above equations of motion. The dependence of the expansion coefficients on  $m$  is fully determined by the radiation pattern of the source used.

Two special cases need to be noted. The first one is for  $l = 0$ . In this case, the toroidal mode is meaningless and it can be derived that  $Y_6 = Y_5/r$  for the spheroidal mode. Accordingly, Eq. (A13) is reduced to a 3D equation system including  $Y_1$ ,  $Y_2$  and  $Y_5$ ,

$$\begin{cases}
 \dot{Y}_1 = -\frac{2\lambda}{(\lambda+2\mu)r}Y_1 + \frac{1}{\lambda+2\mu}Y_2, \\
 \dot{Y}_2 = \left[-\rho\omega^2 - \frac{4\rho g}{r} + \frac{4\mu(3\lambda+2\mu)}{(\lambda+2\mu)r^2}\right]Y_1 - \frac{4\mu}{(\lambda+2\mu)r}Y_2, \\
 \dot{Y}_5 = 4\pi G\rho Y_1.
 \end{cases} \tag{A14}$$

Note that  $Y_5$  is hierarchically coupled with  $Y_1$  and  $Y_2$  in Eq. (A14). Accordingly,  $Y_1$  and  $Y_2$  be solved independently from  $Y_5$ .

The other special case is for  $\mu = 0$ , i.e., for a liquid medium such as the outer core, the ocean or the atmosphere, where the shear stress vanishes ( $Y_4 = 0$ ) and the toroidal mode does

not exist (no shear waves). According to Eq. (A13), the vanishing of  $\mu$  and  $Y_4$  leads to the relation

$$\rho g Y_1 - Y_2 - \rho \omega^2 r Y_3 - \rho Y_5 = 0, \quad (\text{A15})$$

and the 6D equation system governing the spheroidal modes is simplified to a 4D equation system,

$$\begin{cases} \dot{Y}_1 = -\frac{2}{r} Y_1 + \frac{1}{\lambda} Y_2 + \frac{l(l+1)}{r} Y_3, \\ \dot{Y}_2 = -\left(\rho \omega^2 + \frac{4\rho g}{r}\right) Y_1 + \frac{l(l+1)\rho g}{r} Y_3 + \frac{(l+1)\rho}{r} Y_5 - \rho Y_6, \\ \dot{Y}_5 = 4\pi G \rho Y_1 - \frac{l+1}{r} Y_5 + Y_6, \\ \dot{Y}_6 = \frac{4\pi G \rho (l+1)}{r} Y_1 - \frac{4\pi G \rho l(l+1)}{r} Y_3 + \frac{l-1}{r} Y_6, \end{cases} \quad (\text{A16})$$

where  $Y_3$  is related to  $Y_1$ ,  $Y_2$  and  $Y_5$  through Eq. (A15). Note that, at the static limit, i.e., when  $\omega \rightarrow 0$ , Eq. (A16) becomes generally unstable because  $\omega$  appears in the denominator of several terms if substituting  $Y_3$  by Eq. (A15). To overcome the problem, Wang (1991) suggested an alternative equation system, which can be obtained by differentiating Eq. (A15).

This new equation system includes  $Y_1$ ,  $Y_3$ ,  $Y_5$  and  $Y_6$  as the independent unknowns,

$$\begin{cases} \dot{Y}_1 = \left(\frac{\rho g}{\lambda} - \frac{2}{r}\right) Y_1 + \left[\frac{l(l+1)}{r} - \frac{\rho \omega^2 r}{\lambda}\right] Y_3 - \frac{\rho}{\lambda} Y_5, \\ \dot{Y}_3 = \frac{1}{r} \left(1 - \frac{N^2}{\omega^2}\right) Y_1 - \frac{1}{r} \left(1 - \frac{N^2 r}{g}\right) Y_3 + \frac{N^2}{\omega^2 g r} Y_5, \\ \dot{Y}_5 = 4\pi G \rho Y_1 - \frac{l+1}{r} Y_5 + Y_6, \\ \dot{Y}_6 = \frac{4\pi G \rho (l+1)}{r} Y_1 - \frac{4\pi G \rho l(l+1)}{r} Y_3 + \frac{l-1}{r} Y_6, \end{cases} \quad (\text{A17})$$

where

$$N^2 = -\frac{g}{\rho} \left( \frac{d\rho}{dr} + \frac{\rho^2 g}{\lambda} \right), \quad (\text{A18})$$

and  $N/2\pi$  is the Brunt-Väisälä frequency. After  $Y_1$ ,  $Y_3$ ,  $Y_5$  and  $Y_6$  have been solved using Eq. (A17),  $Y_2$  is determined by Eq. (A15). In the Earth outer core and ocean, the so-called Adam-Williamson condition, i.e.,  $N^2 = 0$ , is approximately satisfied. In the Earth atmosphere,

$N^2 > 0$  and the Brunt-Väisälä frequency ranges between 1.75 and 3.68 mHz based on the US standard model. It can be seen that generally no stable solution can be determined for Eq. (A17) at the static limit. In practice, however, static deformation makes sense only within the solid Earth. For numerical convenience, one can modify  $N^2$  so that it becomes frequency-dependent below a critical frequency  $f_o$ , which is equal to or smaller than the real Brunt-Väisälä frequency. For example,

$$N^2(f) = \begin{cases} N_o^2 \sin^{2+\alpha} \left( \frac{\pi f}{2f_o} \right), & \text{for } f < f_o, \\ N_o^2, & \text{for } f \geq f_o, \end{cases} \quad (\text{A19})$$

where  $\alpha \geq 0$  and  $N_o^2$  is calculated using Eq. (A18). At the static limit, Eq. (A17) becomes a stable system because the singularity caused by the terms including the ratio  $N^2/\omega^2$  is thereby avoided.

The boundary conditions to be satisfied by the generalized displacement-stress vector can be derived consistently from Eqs. (A4) – (A6). For each wedged solid to solid interface, the continuity condition is valid for all components of both toroidal and spheroidal displacement-stress vectors.

Since the toroidal motion can be excited only in a solid sub-system where the source is located, its boundary condition is given by  $X_2 = 0$  at the free solid Earth surface, the core-mantle boundary and the inner core boundary.

For the spheroidal motion of degree  $l = 0$ , the displacement-stress vector is continuous everywhere. For  $l > 0$ , however, some attentions should be paid to the conditions at frictionless interfaces like from solid to liquid, from liquid to solid, or from liquid to liquid. In the propagator algorithm, it needs generally to propagate 3 independent displacement-stress vectors simultaneously through each solid layer and 2 through each liquid layer. At an interface from solid to liquid, the 3 vectors on the solid side are linearly combined to 2 vectors to satisfy the vanishing shear stress condition ( $Y_4 = 0$ ). The latter 2 vectors will be propagated

further in the liquid layer. At an interface from liquid to solid, the 2 vectors on the liquid side are continued to the solid side and a third vector will be generated in the form like  $\mathbf{Y} = (0,0,c,0,0,0)^T$ , where  $c$  is the third constant of integration representing a net jump in the horizontal displacement there. Finally, at an interface from liquid to liquid with density discontinuity, each of the 2 independent vectors should be allowed to include a jump in the horizontal displacement to satisfy the continuity condition of the normal stress given by Eq. (A15).

In addition, a special attention should be paid to the boundary conditions for both toroidal and spheroidal motions of degree  $l = 1$ . In this case, the rigid rotation of the Earth and the translational motion of the centre of the Earth become unconstrained by the boundary conditions described above when  $f \rightarrow 0$ . Consequently, numerical instabilities may arise at very low frequencies. The difficulty can be overcome by using the centre of mass system, in which the law of conservation of linear and angular momentum is valid.

For the spheroidal motion of degree  $l = 1$ , one of the surface conditions,  $Y_6(a) = 0$ , needs to be modified to  $Y_5(a) = 0$ . For any internal force like an earthquake,  $Y_5(a) = 0$  for degree degree  $l = 1$  is a logical consequence in the centre of mass system and the two alternative surface conditions are equivalent. For an external force like a meteorite impactation, however,  $Y_5(a)$  and  $Y_6(a)$  cannot vanish simultaneously. If the condition  $Y_5(a) = 0$  is chosen, it is generally expected that  $Y_6(a) \neq 0$ , implying that the centre of mass system is non-inertial under the external forcing.

Similarly, the rigid rotation should be avoided when calculating the toroidal motion of degree  $l = 1$ . In principle, only an external force can result in a net moment acting on the Earth, which is represented by a jump of shear stress ( $X_2$ ) at the source level. In this case, the angular momentum is no more a conserved quantity. In the centre of mass system, it is therefore necessary to require the continuity of shear stress at the source level, or equivalently to require that



$$\int_0^a \rho r^3 X_1 dr = 0, \tag{A20}$$

implying the conservation of angular momentum, where the integral can be carried out simultaneously with Eq. (A12).

## References

- Al-Attar, D., and Woodhouse J.H., 2008. Calculation of seismic displacement fields in self-gravitating earth models - applications of minors vectors and symplectic structure. *Geophys. J. Int.*, **175**, 1176-1208.
- Bouchon, M., 1979. Discrete wave number representation of elastic wave fields in three space dimensions, *J. Geophys. Res.*, **84**, 3609-3614.
- Chapman, C. H., 2003. Yet another elastic plane-wave, layer-matrix algorithm, *Geophys. J. Int.*, **154**, 212-223.
- Chapman, C.H., and Phinney, R.A., 1972. Diffracted seismic signals and their numerical solution, *Meth. Comp. Phys.*, **12**, 165-230.
- Crossley, D.J., 1993. Eigensolutions and seismic excitation of the Slichter mode triplet for a fully rotating earth model. *EOS*, **73**, 60.
- Crossley, D., Rochester, M.J., and Peng, Z.R., 1992. Slichter modes and Love numbers. *Geophys. Res. Lett.*, **91**, 755-794.
- Dahlen, F.A., 1972. Elastic dislocation theory for a self-gravitating elastic configuration with an initial static stress field, *Geophys. J. R. Astron. Soc.*, **28**, 357-383.
- Dahlen, F.A., and Sailor, R., 1979. Rotational and elliptical splitting of the free oscillations of the earth, *Geophys. J. R. Astr. Soc.*, **58**, 609-623.
- Dahlen, F.A., and Tromp, J., 1998. *Theoretical Global Seismology*, Princeton University Press, Princeton.
- Dziewonski, A.M., and Anderson, D.L., 1981. Preliminary reference Earth model. *Phys. Earth planet. Inter.*, **25**, 297-356.
- Dunkin, J.W., 1965. Computation of modal solutions in layered, elastic media at high frequencies, *Bull. Seism. Soc. Am.*, **55**, 335-358.
- Friederich, W., and Dalkolmo, J., 1995. Complete synthetic seismograms for a spherically symmetric earth by a numerical computation of Green's function in the frequency domain, *Geophys. J. Int.*, **122**, 537-550.

- Fuchs, K., 1968. The reflection of spherical waves from transition zones with arbitrary depth-dependent elastic moduli and density, *J. Phys. Earth*, **16**, 27-41.
- Fuchs, K., and Müller, G., 1971. Computation of synthetic seismograms with the reflectivity method and comparison with observation, *Geophys. J. R. astr. Soc.*, **23**, 417-433.
- Gilbert, F., and Backus, G., 1966. Propagator matrices in elastic wave and vibration problems, *Geophysics*, **31**, 326-332.
- Gilbert, F., and Backus, G., 1968. Elastic-gravitational vibrations of a radially stratified sphere, in: *Dynamics of Stratified Solids*, edited by G. Herrmann, American Society of Mechanical Engineers, New York, 82-95.
- Heimann, S., González, Á., Wang, R., Cesca, S., and Dahm, T., 2013. Seismic characterization of the Chelyabinsk meteor's terminal explosion, *Seism. Res. Lett.*, **84**, 1021-1025.
- Hinderer, J., Crossley, D., and Jensen, O., 1995. A search for the Slichter triplet in superconducting gravimeter data, *Phys. Earth Plan. Int.*, **90**, 183-195.
- Hoechner, A., Babeyko, A.Y., and Sobolev, S.V., 2008. Enhanced GPS inversion technique applied to the 2004 Sumatra earthquake and tsunami, *Geophys. Res. Lett.*, **35**, L08310, doi:10.1029/2007GL033133.
- Ivan, M., Ghica, D.V., Gosar, A., Hatzidimitriou, P., Hofstetter, R., Polat, G., and Wang, R., 2015. Lowermost mantle velocity estimations beneath the central North Atlantic area from Pdif observed at Balkan, East Mediterranean, and American stations, *Pure and Applied Geophysics*, **172**, 283-293.
- Ivan, M., and Wang, R., 2013. Anomalous high amplitude ratios of P5KP/PKPab and P4KP/P(S)cP observed globally around 1 Hz, *J. Seismol.*, **17**, 453-464.
- Kanamori, H., and Anderson, D.L., 1977. Importance of physical dispersion in surface waves and free oscillation problems. *Rev. Geophys. Space Phys.*, **15**, 105-112.
- Kawai, K., Takeuchi, N., and Geller, R.J., 2006. Complete synthetic seismograms up to 2 Hz for transversely isotropic spherically symmetric media, *Geophys. J. Int.*, **164**, 411-424.
- Kennett, B.L.N., 1983. *Seismic Wave Propagation in Stratified Media*, Cambridge University Press, Cambridge.

- Kennett, B.L.N., Engdahl, E.R., and Buland, R., 1995. Constraints on seismic velocities in the Earth from travel times, *Geophys. J. Int.*, **122**, 108-124.
- Kind, R., 1983. Improvements to layer matrix method, *J. Geophys.*, **53**, 127-130.
- Knopoff, L., 1964. A matrix method for elastic wave problems, *Bull. Seism. Soc. Am.*, **54**, 431-438.
- Komatitsch, D., and Tromp, J., 1999. Introduction to the spectral-element method for 3-D seismic wave propagation, *Geophys. J. Int.*, **139**, 806-822.
- Lognonné, P., Clévéde, E., and Kanamori, H., 1998. Computation of seismograms and atmospheric oscillations by normal mode summation for a spherical Earth model with realistic atmosphere, *Geophys. J. Int.*, **135**, 388 - 406.
- Ma, Y., Wang, R., and Zhou, H., 2012. A note on the equivalence of three major propagator algorithms for computational stability and efficiency, *Earthq. Sci.*, **25**, 55-64.
- Masters, G., Barmine, M., and Kientz, S., 2011. *Mineos – User Manual Version 1.0.2*, [www.geodynamics.org](http://www.geodynamics.org).
- Motagh, M., Schurr, B., Anderssohn, J., Cailleau, B., Walter, T.R., Wang, R., and Villotte, J.P., 2010. Subduction earthquake deformation associated with 14 November 2007, Mw 7.8 Tocopilla earthquake in Chile: Results from InSAR and aftershocks, *Tectonophysics*, **490**, 60-68.
- Müller, G., 1977. Earth-flattening approximation for body waves derived from geometric ray theory - improvements, corrections and range of applicability, *J. Geophys.*, **42**, 429-436.
- Müller, G., 1983. Rheological properties and velocity dispersion of a medium with a power-law dependence of Q on frequency, *J. Geophys.*, **54**, 20-29.
- Müller, G., 1985. The reflectivity method: a tutorial, *J. Geophys.*, **58**, 153-174.
- Ochi Y., Fujita, K., Niki, I., Nishimura, H., Izumi, N., Sunahara, A., Naruo, S., Kawamura, T., Fukao, M., Shiraga, H., Takabe, H., Mima, K., Nakai, S., Uschmann, I., Butzbach, R., Forster, E., Courtier, N., Ducarme, B., Goodkind, J., Hinderer, J., Imanishi, Y., Seama, N., Sun, H., Merriam, J., Bengert, B., and Smylie, D.E., 2000. Global superconducting gravimeter observations and the search for the translational modes of the inner core, *Phys. Earth and Plan. Int.*, **117**, 3-20.
- Okada, Y., 1992. Internal deformation due to shear and tensile faults in a half-space, *Bull. Seism. Soc. Am.*, **82**, 1018-1040.

- Okubo, S., 1993. Reciprocity theorem to compute the static deformation due to a point dislocation buried in a spherically symmetric earth, *Geophys. J. Int.*, **115**, 921-928.
- Peng, Z.R., 1997. Effects of a mushy transition zone at the inner core boundary on the Slichter modes, *Geophys. J. Int.*, **131**, 607-617.
- Pollitz, F.F., 1992. Postseismic relaxation theory on the spherical Earth, *Bull. Seism. Soc. Am.*, **82**, 422-453.
- Pollitz, F.F., 1997. Gravitational viscoelastic postseismic relaxation on a layered spherical earth, *J. Geophys. Res.*, **102**, 17921-17941.
- Raveloson, A., Wang, R., Kind, R., Ceranna, L., and Yuan, X., 2012. Brief communication “Seismic and acoustic-gravity signals from the source of the 2004 Indian Ocean Tsunami”, *Nat. Hazards Earth Syst. Sci.*, **12**, 287-294.
- Rieutord, M., 2002. Slichter modes of the Earth revisited, *Phys. Earth Planet. Inter.*, **131**, 269-278.
- Rogister, Y., 2003. Splitting of seismic-free oscillations and of the Slichter triplet using the normal mode theory of a rotating, ellipsoidal Earth. *Phys. Earth Planet. Inter.*, **140**, 169-182.
- Rosat, S., Rogister, Y., Crossley, D., and Hinderer, J., 2006. A search for the Slichter triplet with superconducting gravimeters: Impact of the density jump at the inner core boundary, *J. Geodynam.*, **41**, 296-306.
- Rundle, J.B., 1980. Static elastic-gravitational deformation of a layered half-space by point couple sources, *J. Geophys. Res.*, **85**, 5354-5363.
- Rundle, J.B., 1981. Vertical displacements from a rectangular fault in a layered elastic-gravitational media, *J. Phys. Earth*, **29**, 173-186.
- Rundle, J.B., 1982. Viscoelastic-gravitational deformation by a rectangular thrust fault in a layered Earth, *J. Geophys. Res.*, **87**, 7787-7796.
- Schurr, B., Asch, G., Hainzl, S., Bedford, J., Hoechner, A., Palo, M., Wang, R., Moreno, M., Bartsch, M., Zhang, Y., Oncken, O., Tilmann, F., Dahm, T., Victor, P., Barrientos, S., and Vilotte, J.P., 2014. Gradual unlocking of plate boundary controlled initiation of the 2014 Iquique earthquake, *Nature*, **512**, 299-302.
- Segall, P., 2010. *Earthquake and Volcano Deformation*, Princeton Univ. Press, Princeton, U. K.

- Slichter, L.B., 1961. The fundamental free mode of the Earth's inner core, *Proc. Natl. Acad. Sci. U.S.A.*, **47**, 186-190.
- Sun, W., and Okubo, S., 1993. Surface potential and gravity changes due to internal dislocations in a spherical earth - I. Theory for a point dislocation, *Geophys. J. Int.*, **114**, 569-592.
- Sun, W., and Okubo, S., 1998. Surface potential and gravity changes due to internal dislocations in a spherical earth - II. Application to a finite fault, *Geophys. J. Int.*, **132**, 79-88.
- Takeuchi, H., and Saito, M., 1972. Seismic surface waves, in: *Methods in Computational Physics*, edited by B.A. Bolt, Academic Press, New York, 217-295.
- Tong, X., Sandwell, D., Luttrell, K., Brooks, B., Bevis, M., Shimada, M., Foster, J., Smalley, R., Parra, H., Báez Soto, J.C., Blanco, M., Kendrick, E., Genrich, J., and Caccamise, D.J., 2010. The 2010 Maule, Chile earthquake: Downdip rupture limit revealed by space geodesy, *Geophys. Res. Lett.*, **37**, L24311, doi:10.1029/2010GL045805.
- van Driel, M., Krischer, L., Stähler, S.C., Hosseini, K., and Nissen-Meyer, T., 2015. Instaseis: instant global seismograms based on a broadband waveform database. *Solid Earth*, **6**, 701-717.
- Wang, R., 1991. *Tidal Deformations on a Rotating, Spherically Asymmetric, Viscoelastic and Laterally Heterogeneous Earth*, European University Studies, Series XVII, Earth Sciences, Vol. 5, Peter Lang, Frankfurt am Main.
- Wang, R., 1997. Tidal response of the solid earth, in *Tidal Phenomena*, edited by H. Wilhelm, W. Zürn and H.G. Wenzel, *Lecture Notes in Earth Sciences*, **66**, 27-57, Springer-Verlag, Berlin/Heidelberg, Germany.
- Wang, R., 1999. A simple orthonormalization method for stable and efficient computation of Green's functions, *Bull. Seism. Soc. Am.*, **89**, 733-741.
- Wang, R., Lorenzo Martín, F., and Roth, F., 2003. Computation of deformation induced by earthquakes in a multi-layered elastic crust - FORTRAN programs EDGRN/EDCMP, *Computers & Geosciences*, **29**, 195-207.
- Wang, R., and Kümpel, H.J., 2003. Poroelasticity: Efficient modelling of strongly coupled, slow deformation processes in a multilayered half-space, *Geophysics*, **68**, 705-717.

- Wang, R., Lorenzo Martín, F., and Roth, F., 2006. PSGRN/PSCMP - a new code for calculating co- and post-seismic deformation, geoid and gravity changes based on the viscoelastic gravitational dislocation theory, *Computers & Geosciences*, **32**, 527-541.
- Wang, R., and Wang, H., 2007. A fast converging and anti-aliasing algorithm for Green's functions in terms of spherical or cylindrical harmonics, *Geophys. J. Int.*, **170**, 239-248.
- Yang, H.Y., Zhao, L., and Hung, S.H., 2010. Synthetic seismograms by normal-mode summation: a new derivation and numerical examples. *Geophys. J. Int.*, **183**, 1613-1632.
- Zhang, Y., Wang, R., Zschau, J., Chen, Y.T., Parolai, S., and Dahm, T., 2014a. Automatic imaging of earthquake rupture processes by iterative deconvolution and stacking of high-rate GPS and strong motion seismograms, *J. Geophys. Res.*, **119**, 5633-5650.
- Zhang, Y., Wang, R., Chen, Y.T., Xu, L., Du, F., Jin, M., Tu, H., and Dahm, T., 2014b. Kinematic rupture model and hypocenter relocation of the 2013 Mw6.6 Lushan earthquake constrained by strong-motion and teleseismic data, *Seism. Res. Lett.*, **85**, 15-22.

## Figures

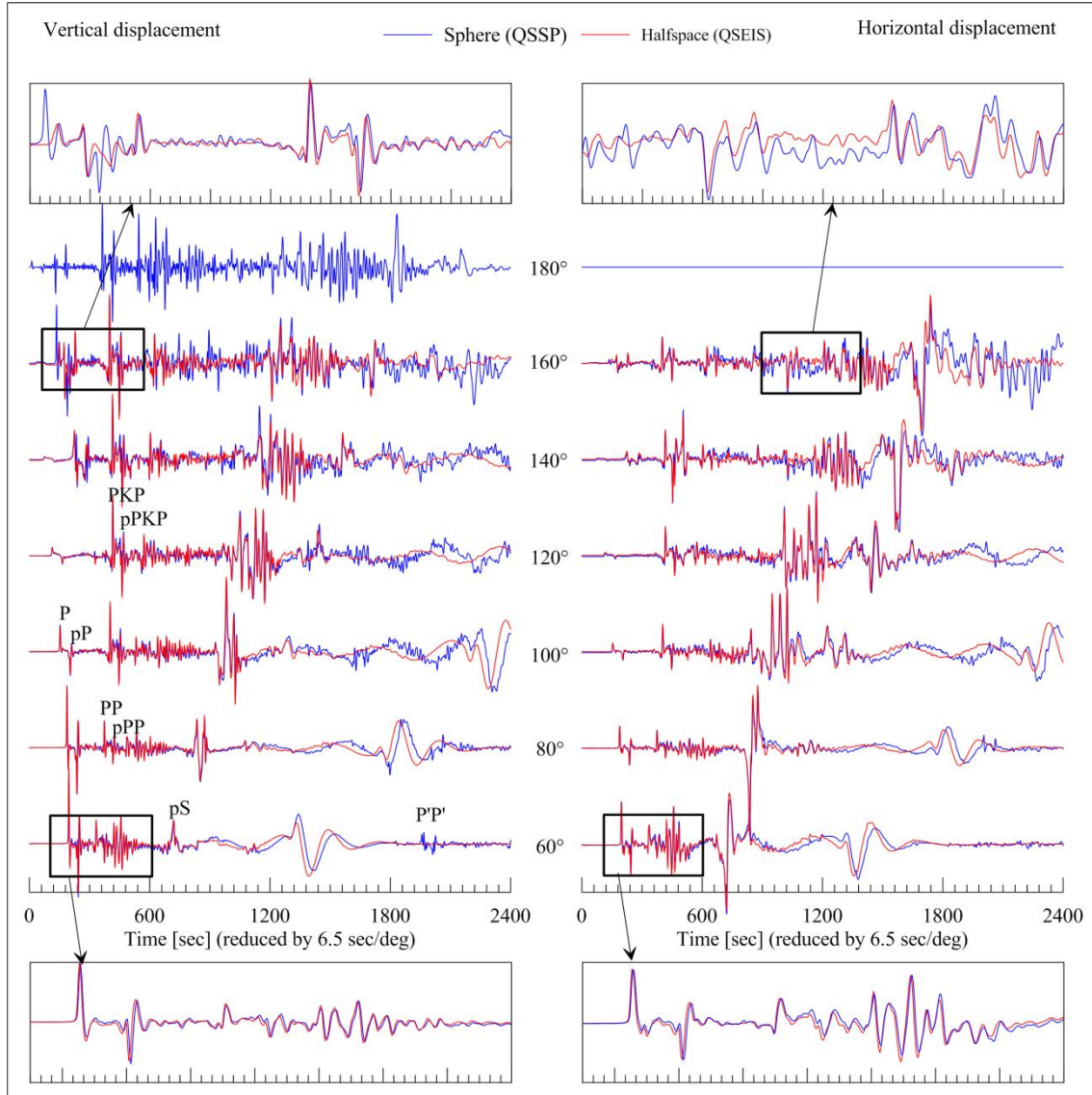


**Figure 1.** Comparison of teleseismic ( $60^{\circ}$ - $180^{\circ}$ ) synthetic seismograms computed using the QSSP code (this study) based on the spherical Earth model AK135 and the QSEIS code (Wang, 1999) based on the corresponding plane-earth model with the earth-flattening transformation. A point explosion source at the depth of 210 km is used. The cut-off frequency is 1.0 Hz. The 4 zoomed windows are selected to show the agreements or disagreements between the results from two different codes more clearly.



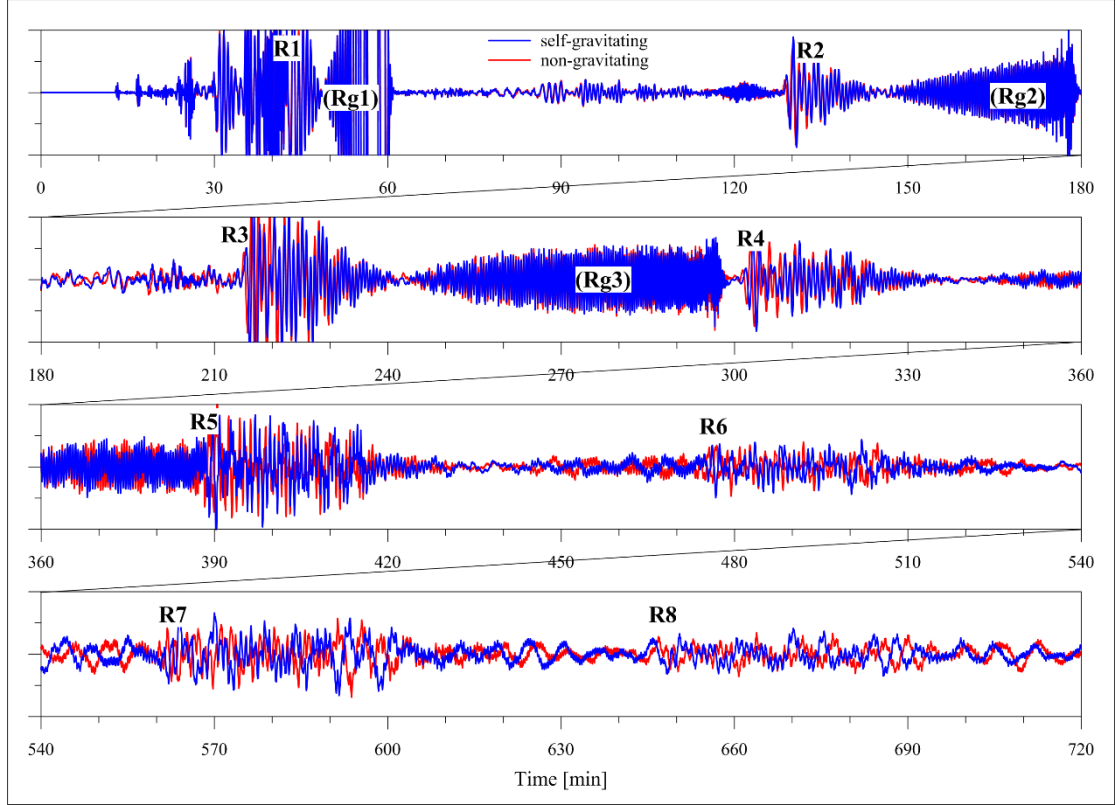


**Figure 2.** Comparison of synthetic broadband seismograms (vertical component) calculated based on the Earth model AK135 with and without the gravity effect. The source is an impulsive strike-slip double-couple at the depth of 33 km, and the observation site is located at the epicentral distance of  $90^\circ$ . The whole time window is 12 h and is divided into four equal sub-windows, each being scaled individually. The cut-off frequency is 0.1 Hz. R1-8 denote the global Rayleigh wave groups.

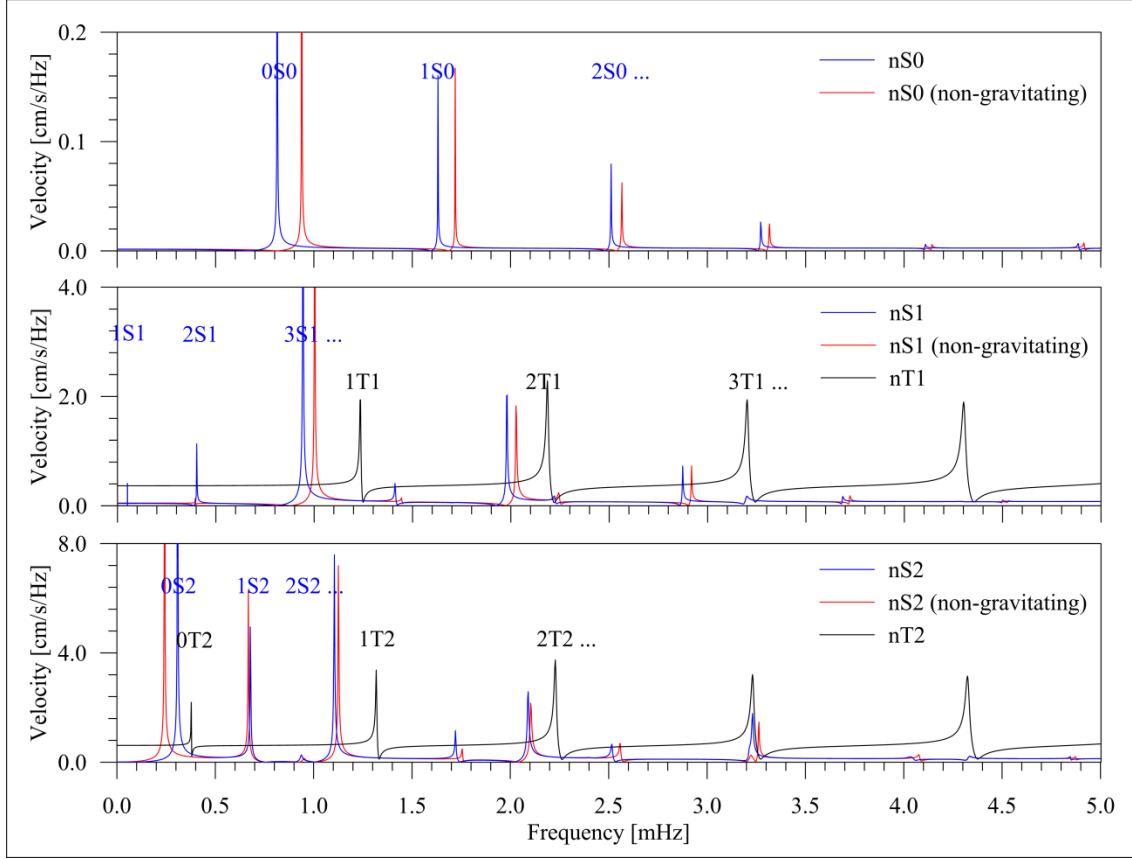


**Figure 3.** Comparison of the Fourier amplitude spectra of free oscillations ( $nS_l$  and  $nT_l$  for  $\leq 2$ ) calculated based on the Earth model PREM with and without the gravity effect. The source is adopted from Harvard's CMT double-couple for the 2004 Mw9.3 Sumatra earthquake, and the observables are the surface velocity as measured by a broadband seismometer located at the epicentre. Note that the resonance peaks become asymmetric if the background spectral level contributed from the neighbouring modes is significant.

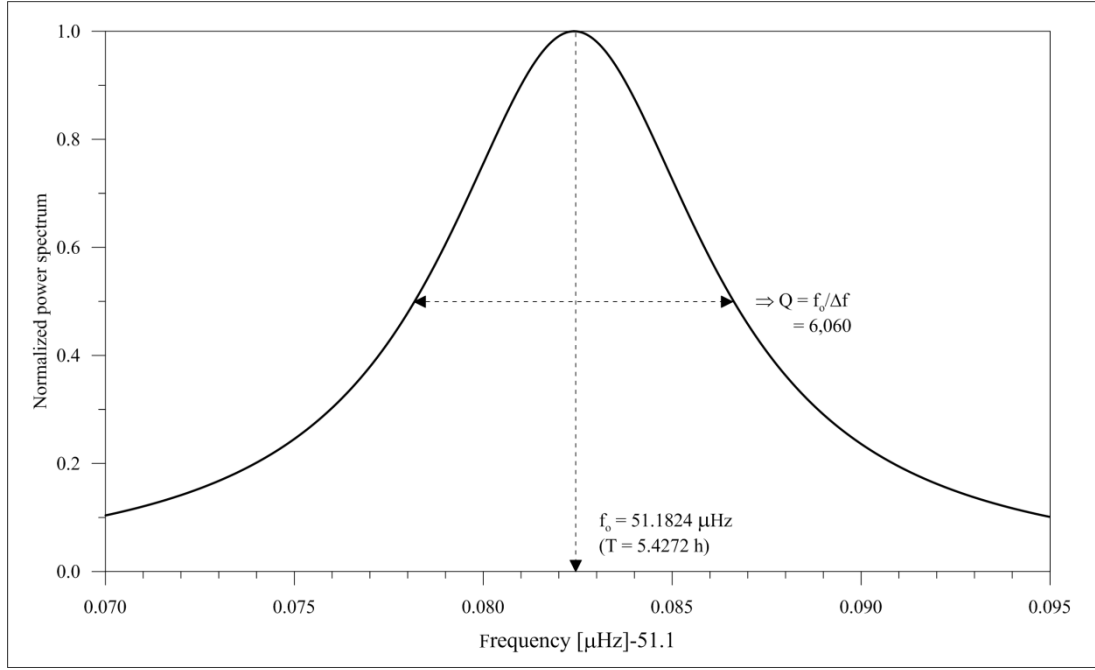


**Figure 4.** Fourier power spectrum around the spheroidal mode 1S1 (Slichter mode) calculated using the Earth model PREM. The source is adopted from Harvard’s CMT double-couple solution for the 2004 Mw9.3 Sumatra earthquake at the depth of 30 km, and the observable is the vertical ocean-bottom velocity at the epicentre.

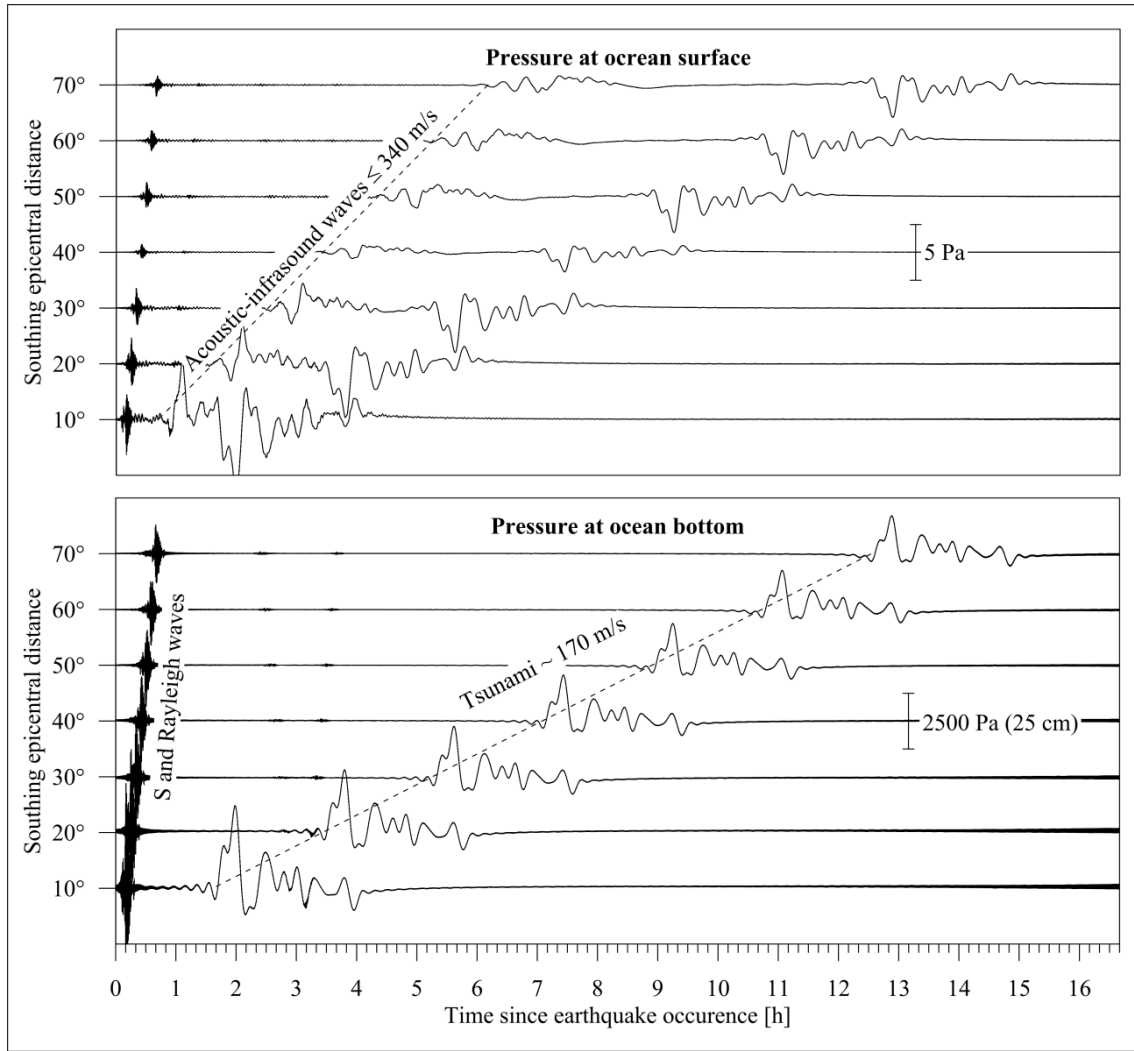


**Figure 5.** Synthetic seismograms for tsunami and infrasound waves caused by the 2004 Mw9.3 Sumatra earthquake. The Earth model used is PREM (with a uniform ocean layer of 3 km) combined with the standard US atmosphere model, the earthquake source consists of 432 sub-faults with the slip distribution adopted from Hoechner et al. (2008), the cut-off frequency is 0.04 Hz, and the receiver profile is southward from the earthquake epicentre.

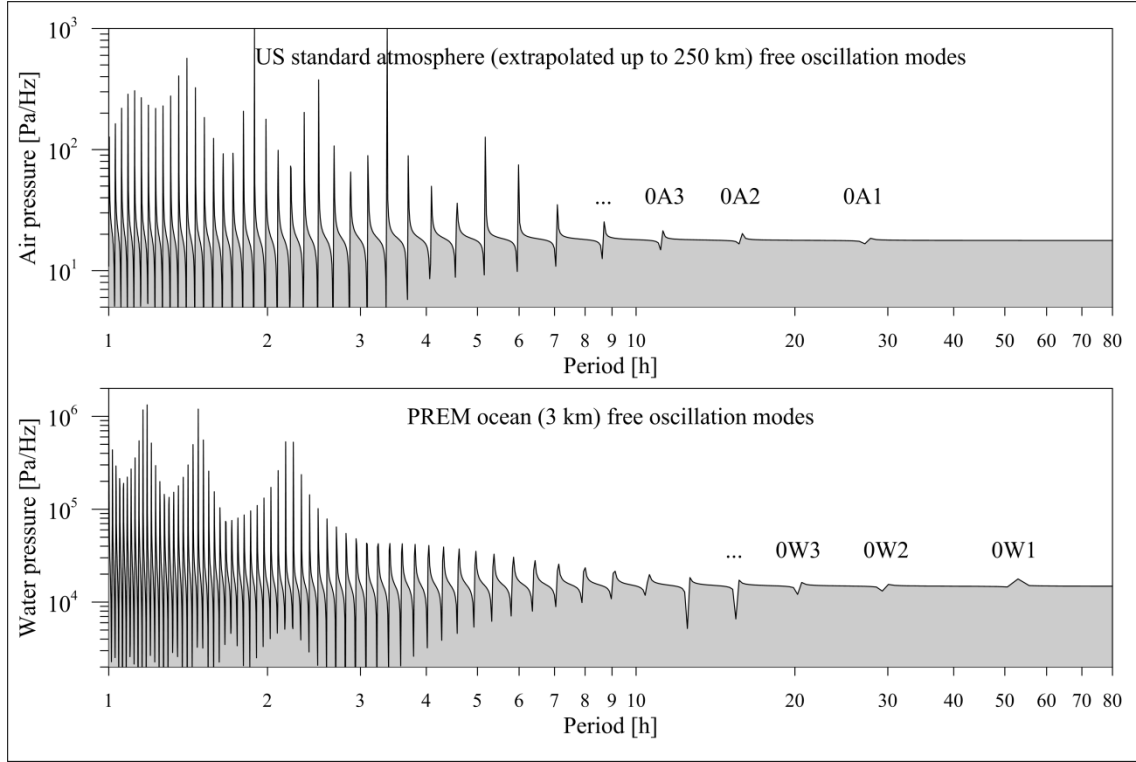


**Figure 6.** Long-period free oscillation modes of the atmosphere and ocean calculated using (1) the US standard atmosphere (extrapolated up to 250 km) combined with the solid Earth model PREM and (2) the PREM model (with 3 km ocean), respectively. The spectra are modulated by the amplitude estimated for the 2004 Mw9.3 Sumatra earthquake.

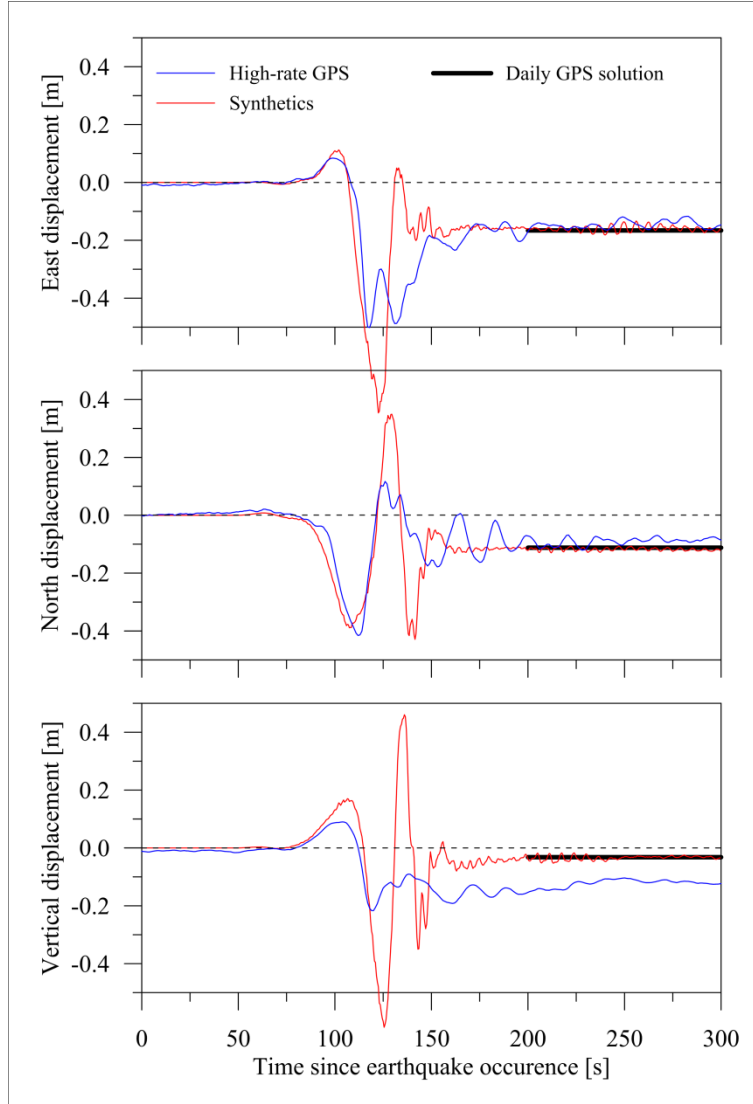


**Figure 7.** Comparison between the high-rate GPS and synthetic displacement seismograms at Station ROBL ( $-32.9760^{\circ}\text{N}$ ,  $-71.0157^{\circ}\text{E}$ ) for the 2010  $M_w 8.8$  Maule (Chile) earthquake. The earthquake source used is the finite-fault model adopted from Tong et al. (2010).

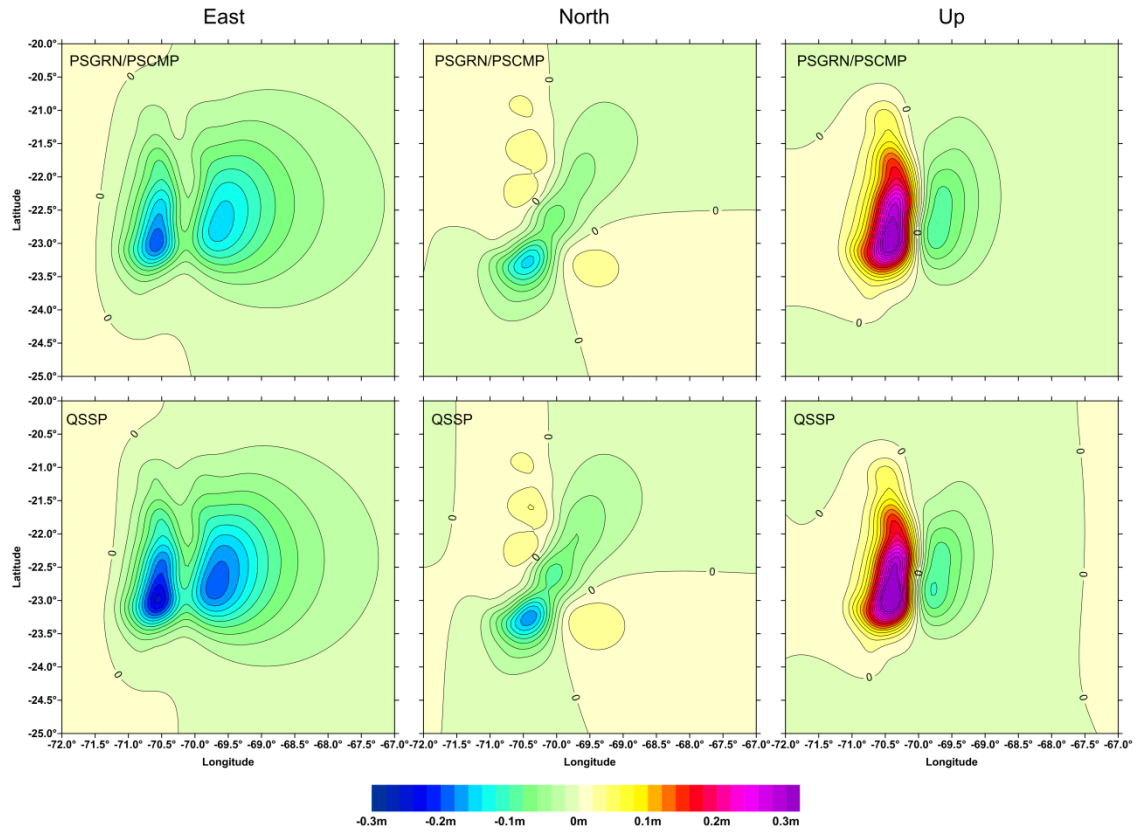


**Figure 8.** Comparison of the static surface displacement fields for the 2007 Mw7.7 Tocopilla (Chile) earthquake calculated using two different codes *QSSP* (this study) and *PSGRN/PSCMP* (Wang et al., 2006). The Earth model used is AK135. The slip model of the earthquake consists of about 1000 fault patches adopted from Motagh et al. (2010).

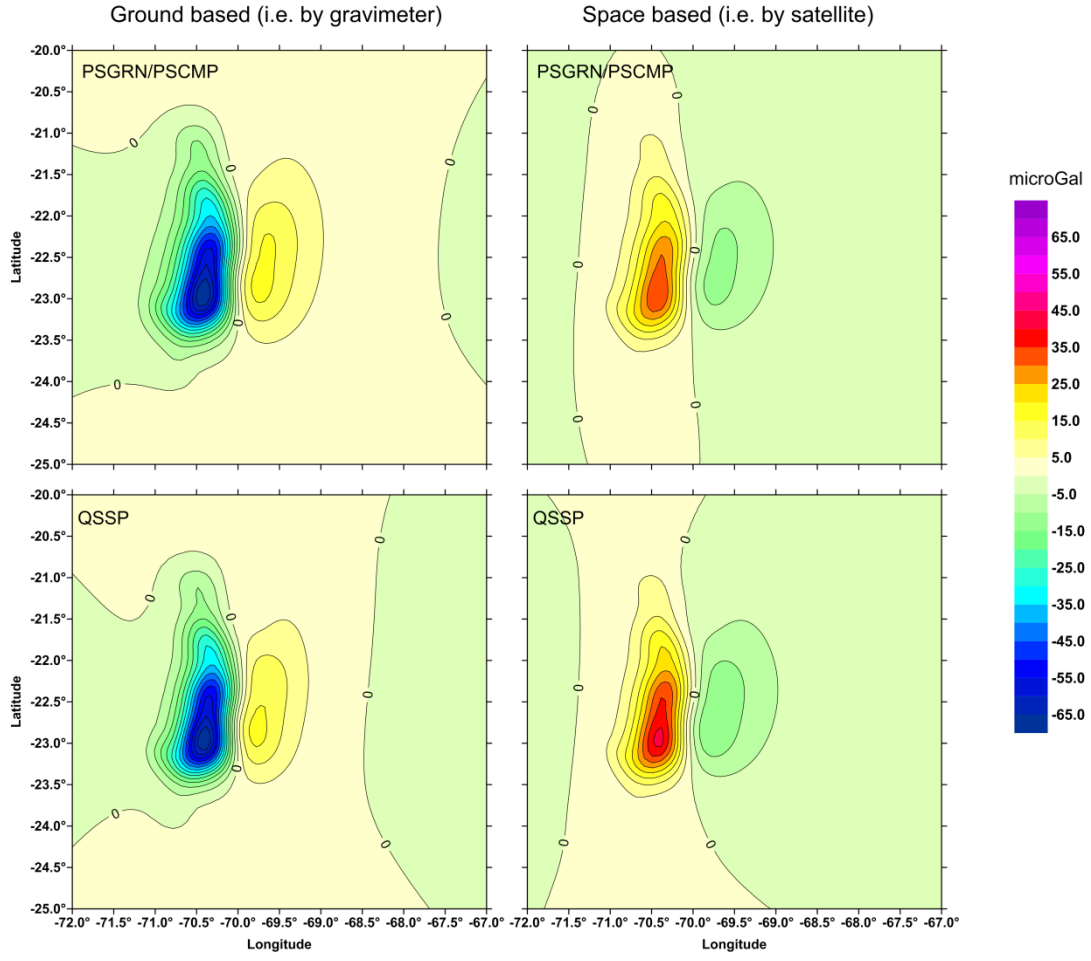


**Figure 9.** Same as Fig. 8, but for changes in the gravity field. Note that the difference between the ground and space based gravity changes is given by the free-air correction  $\delta g_f = -\frac{2}{R} g_o u_r$ , where  $R$  is Earth's radius,  $g_o$  is Earth's surface gravity, and  $u_r$  is the vertical surface displacement.